Distant Retrograde Orbits for Space-based Near Earth Objects Detection

Michele Stramacchia
Astronautics, Aeronautics and Computational Engineering Unit, University of Southampton, SO171BJ, UK

Camilla Colombo[1]
Astronautics, Aeronautics and Computational Engineering Unit, University of Southampton, SO171BJ, UK

Franco Bernelli-Zazzera
Department of Aerospace Science and Technology, Politecnico di Milano, 20156 Milano, Italy

We analyse a concept for the detection of Potentially Hazardous Asteroids (PHAs) from a space-based network of telescopes on retrograde distant periodic orbits. Planar periodic orbits are designed in the Sun-Earth circular restricted three-body problem, starting from initial conditions in the Hill's problem available from the literature. A family of retrograde orbits centred at the Earth is selected as baseline, based on their maximum distance from Earth, larger than the Earth-L_2 distance. Indeed, spacecraft on such orbits can detect PHAs incoming from the Sun direction, which could not otherwise be monitored from current Earth-based systems. A trade-off on the orbit amplitude, asteroid diameter to be detected, and the constellation size is performed considering current visible sensor telescope technology. The Chelyabinsk meteor scenario is studied and the potential warning time that could be gained with a space-based survey system with respect to an Earth based-survey system is shown.

1 Introduction

The international interest towards Near Earth Objects (NEOs) is growing because of the increased awareness of the danger some asteroids or comets pose to the Earth. Potentially Hazardous Asteroids (PHAs) have the potential to make a close approach to the Earth and a size large enough to cause significant regional or global damage in the event of an impact (Belton, 2004). Telescopes' ability to detect NEOs depends on their distance from the observer, size,

[1] Corresponding author. *Email address*: c.colombo@soton.ac.uk

albedo and their position relative to the Sun. Ground-based telescopes, operating in various ranges of the electromagnetic spectrum, can span about 2 steradians (sr) portion of the celestial sphere (Stokes, 2003, Stokes et al., 2002). The opposition region has proven to be the most profitable area of the sky to search for NEOs, because of objects relative position with respect to the Sun. Since they have a smaller solar phase angle, it is very easy discriminating NEOs from other asteroids; moreover, astrometry observations are most powerful due to small geocentric distances (Michelsen, 2004). Because the sky regions next to the Sun direction are difficult to observe, it may be important to have two or more ground-based telescopes widely spaced in latitude. From the ground, the near Sun regions are only observable for a small fraction of the night. Several search programs (Stokes et al., 2002, Perna et al., 2013, Vereš et al., 2009) have been undertaken to map the entire population of NEOs, among them the Spaceguard Survey catalogued 90% of NEOs with diameter larger than 1 km.

However, if a Tunguska-class or smaller NEO approaches the Earth from the Sun direction, its observation from ground is very difficult or even impossible, this was the case of the meteorite fall in Chelyabinsk, Russia, in February 2013 (Zuluaga and Ferrin, 2013, Andronikov et al., 2014). Because the sky region next to the Sun direction is difficult to observe, space-based systems can integrate ground-based observation for monitoring NEOs from a location in between the Sun and the Earth (Stokes, 2003, Perna et al., 2013). Space-based systems can access a larger portion of the sky with respect to ground-based systems and background noise is reduced due to the lack of atmosphere. This at higher mission cost for launch of large telescopes, orbit injection, maintenance, cost for ensuring appropriate thermal and pointing conditions for observations, data processing and down-link to Earth.

Current and future projects for NEO space-based observation are the Near-Earth Object Surveillance Satellite in an Earth-centred sun-synchronous orbit (Stokes, 2003) and the Sentinel mission in a Venus-like orbit[2]. A constellation on sun-synchronous 800 km altitude orbits can cover 2 sr of the total sky at any time, but in opposite hemi-spheres during each half orbit. The Sun exclusion zone is about 40 degrees half angle from the Sun–Earth line and the telescope must also avoid pointing too close to the Earth. LEO-based observation is the lowest cost space mission, because it does not need on-board propulsion to get into the final orbit and it enables high downlink data rates with a low power communication sub-system; however, orbit maintenance manoeuvres are required. Alternatively, spacecraft at the Sun–Earth Libration point L_2 can view the full sky except for the approximately 40 degree half angle cone centred at the Sun. It needs a capable launch vehicle, on-board propulsion and large Deep Space Network antennas for tracking

[2] Sentinel Mission: http://sentinelmission.org/sentinel-mission/ [Last retrieved 30/10/2014]

and data downlink (Stokes, 2003). Spacecraft at the Sun-Earth Libration point L_1 can view a smaller sky portion with respect to spacecraft at L_2, as there are two exclusion zones due to the Earth and Sun's position; however, L_1 is an excellent position because all approaching asteroids may be viewed repeatedly with a good phase angle and hence with a good visual magnitude (Stokes, 2003, Dunham et al., 2013). Recently, the Sentinel mission was proposed on a heliocentric Venus-like orbit with semi-major axis of 0.7 AU, from where NEOs could be observed with a smaller solar phase angle near opposition. From this orbit, Aten asteroids can be discovered that spend most of their time inside 1 AU. The major drawback of this Venus-like orbit solution is the great difference in heliocentric longitude between the spacecraft and the Earth. In fact, the heliocentric longitude goes from 0 to 180 degrees, making communication difficult and hence impairing the ability to communicate imminent hazardous objects.

An alternative solution is to place a space telescope on a Distant Retrograde Orbit (DRO). DROs is a family of periodic orbits that arise from the numerical exploration of the Hill's limiting case of the Circular Restricted Three Body Problem (CR3BP) (Hénon, 1969, Mingotti et al., 2010). Valsecchi et al. (Valsecchi et al., 2012) firstly proposed to place a 3-spacecraft constellation on DROs, however no further study was performed on assessing the detection capabilities from such orbits and investigating the relation between the orbit amplitude and the size of the constellation in terms of number of spacecraft and coverage area.

In this article, the feasibility of a spacecraft constellation for NEOs detection from a family of Distant Retrograde Orbits in the Sun – (Earth + Moon) system is studied. DROs can reach a minimum distance from the Earth larger than the Earth–L_2 distance. DROs belong to the larger family of Distant Period Orbits (DPOs), studied by Hénon (Hénon, 1997, Hénon, 1969) in the Hill's problem, the particular case of the CR3BP where the mass parameter tends to zero (Meyer et al., 2009). These orbits received the attention of the astrodynamics community(Demeyer and Gurfil, 2007, Woolley and Scheeres, 2010, Xue and Junfeng, 2013, Mingotti et al., 2010) because they are ideal for space-based telescopes that need to be far from the Earth to avoid the near Earth environmental effects, yet need to remain bounded within some pre-defined distance for communication purposes. Moreover, DPOs are ideal for solar storm warning systems that can provide longer warning times than those available from a similar system at the interior Libration points of the Sun – (Earth + Moon) system (Kechichian et al., 2005, Demeyer and Gurfil, 2007).

In this work, we are interested in families of periodic orbits around the secondary body. Due to the large distance they reach from Earth, larger than the Earth–L_2 distance, DPOs can be selected as operational orbits for space observation of PHAs. Indeed, from these orbits, spacecraft carrying visible band telescopes can monitor and protect

the space surrounding the Earth. In particular, since part of the orbit is spent in between the Earth and the Sun, it is possible to cover a region of space that is usually forbidden using ground-based telescopes (being in the direction of the Sun, therefore not observable with optical instruments). This allows monitoring asteroids that may intersect the Earth on a trajectory that comes from the Sun-Earth direction and thus increasing the warning time before a possible re-entry in the Earth's atmosphere (Valsecchi et al., 2012).

Starting from the initial conditions in the Hill's model, four families of simple periodic orbits around the second primary and the L_1 and L_2 Libration points (Hénon, 1969) are analysed. A differential correction algorithm (Koon et al., 2011, Bernelli Zazzera et al., 2004, Scott and Spencer, 2010), coupled with numerical continuation method (Koon et al., 2011), is employed to refine the orbits in the Sun – (Earth + Moon) planar CR3BP. The complete map of periodic orbits in the energy–amplitude plane is built to classify them in terms of distance and velocity from the second primary and orbit period. Based on this, the family-*f* of retrograde orbits, Distant Retrograde Orbits, is selected as operational orbits for space observation of PHAs.

An analytical model for asteroid detection (Binzel et al., 1989, Belton, 2004, Michelsen, 2004, Buchheim, 2010, Sanchez and Colombo, 2013) is used to assess the observation capabilities of spacecraft on DROs in terms of smallest asteroid size from a given orbit as function of distance, solar phase angle, asteroid albedo, for a fixed visual magnitude. A set of heart-shaped contour curves are computed to identify the minimum asteroid size that can be observed from a given orbit and the geometric coverage of the sky region, in particular the added domain within the exclusion zone of current Earth-based systems, when the spacecraft is at the inferior conjunction position. Then, if more than one spacecraft are placed on an orbit, the spatial envelope coverage area can be numerically computed. A trade-off on the number of spacecraft within the constellation and the orbit amplitude for a certain asteroid size to be detected is performed. The orbit selection is then made through an optimisation process to assure for each orbital spacecraft configuration the spatial envelope feasibility (i.e., spatial envelope without blind zone), considering the asteroid diameter and constellation size as input parameters. Finally, the Chelyabinsk asteroid's is considered as a test scenario, to show the warning time that could be gained with a space based survey system respect to an Earth survey system. The results show that the warning time is affected by the relative geometry between the asteroid trajectory and the spacecraft configuration. Moreover, the spacecraft configuration is influenced by the constellation size, which in turn affects the mission cost.

The paper is organised as follows: Section 2 summarises the dynamical models of the CR3BP and the Hill's problem used for the orbit selection and design in Section 3. Section 4 analyses the feasibility of a telescope network for NEO detection. To this aim, the astronomical model used is first introduced and the metrics to assess the feasibility of the constellation are defined and calculated. The sensitivity of these metrics to the orbit size, spacecraft number for the space-based survey system is presented. Finally, the mission case for the detection of the Chelyabinsk meteoroid is shown in Section 5 and some conclusion are drafted in Section 6.

2 Dynamical models

The dynamical models used for the orbit and trajectory design are the CR3BP of the Sun and the Earth-Moon barycentre, in its Planar form (PCR3BP) (Szebehely, 1967, Vinti et al., 1998, Battin, 1999, Murray and Dermott, 1999, Koon et al., 2011, Meyer et al., 2009), and the Hill's model (Szebehely, 1967, Hénon, 1969).

2.1 Planar Circular Restricted Three-Body Problem

The CR3BP models the motion of a spacecraft (i.e., massless particle) under the gravitational attraction of two point masses m_1 and m_2 revolving around their common centre of mass on circular orbits. We further restrict the motion of the spacecraft to be in the orbital plane defined by the two primaries (PCR3BP). In what follows, we will consider three different reference systems, the synodic, the sidereal and Hill' system. The synodic system is centred at the centre of mass of m_1 and m_2, and rotates with constant angular velocity around it. Figure 1 shows the geometry of the problem (Murray and Dermott, 1999, Koon et al., 2011): *x* and *y* are the coordinates in the synodic rotating system (i.e., black system), whereas *X* and *Y* represent the position in the inertial or sidereal system (i.e., grey system). The synodic system is adimensionalised with units of length equal to $r_0 = 1\,\mathrm{AU}$, unit of time equal to $\tau_0 = \sqrt{AU^3/\left(\mu_{\mathrm{Sun}} + \mu_{\mathrm{Earth}} + \mu_{\mathrm{Moon}}\right)}$, and unit of velocity equal to $v_0 = r_0/\tau_0$. If we introduce the mass parameter for the planetary system $\mu = m_2/(m_1 + m_2)$ [3], the normalised position of the primary bodies in the synodic system can be defined as $x_1 = -\mu$ and $x_2 = 1-\mu$. Table 1 summarises the characteristic values of the Sun – (Earth + Moon) system that combines the Earth and Moon into the second primary.

[3] Note that μ_{Sun}, μ_{Earth}, and μ_{Moon} are the standard gravitational parameter of Sun, Earth and Moon respectively, used in the two-body problem and measured in $m^3 s^{-2}$ (i.e. the product of the gravitational constant G and the mass M of the celestial body), while μ is the dimensionless mass parameter used in the three-body problem.

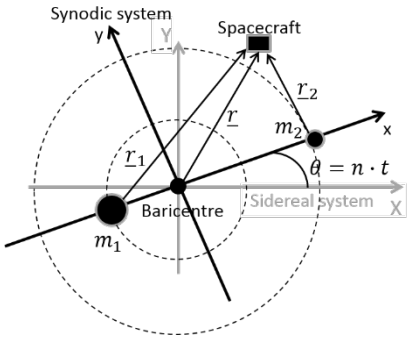

Figure 1. Geometry for the PCR3BP.

Table 1. Characteristic values for the Sun – (Earth + Moon) planetary system.

μ	r_0 [km]	v_0 [km]	τ_0 [rad/s]
3.04014735e-6	1.496e8	29.784	5.0086e6

The equations of motion for the spacecraft in the field of PCR3BP are well known (Murray and Dermott, 1999, Koon et al., 2011, Szebehely, 1967):

$$\begin{cases} \ddot{x} - 2n\dot{y} = \dfrac{\partial \bar{\Omega}(x,y)}{\partial x} \\ \ddot{y} + 2n\dot{x} = \dfrac{\partial \bar{\Omega}(x,y)}{\partial y} \end{cases} \tag{1}$$

where $n = 1$ is the normalised angular velocity for the synodic system with respect to the sidereal system and $\bar{\Omega}(x,y)$ is the pseudo-potential composed by the centrifugal potential and gravitational potential as:

$$\bar{\Omega}(x,y) = \frac{1}{2} n^2 \left(x^2 + y^2\right) + \frac{1-\mu}{r_1} + \frac{\mu}{r_2} \tag{2}$$

with r_1 and r_2 the distances of the spacecraft from m_1 and m_2 respectively. The scalar field in Eq. (2) influences the equations of motion through its gradient, so we can introduce in its expression a constant term that allows obtaining a more symmetric form for the pseudo-potential (Szebehely, 1967)[4]:

$$\Omega(x,y) = \bar{\Omega}(x,y) + \frac{1}{2}(1-\mu)\mu \tag{3}$$

[4] Note that the advantage of adding the symmetric term $\frac{1}{2}(1-\mu)\mu$ in Eq. (3) and (4) is that, in this way, the value of J calculated at the Libration points L_4 and L_5 becomes independent from the mass parameter μ, that is, from the planetary system under analysis: $J(L_4) = J(L_5) = 3$. This allows a simplified comparison among different planetary systems.

Eqs. (1) have an integral of motion, the Jacobi integral, which expresses the conservation of energy in the relative motion of the spacecraft:

$$J\left(x, y, \dot{x}, \dot{y}\right) = -\left(\dot{x}^2 + \dot{y}^2\right) + n^2\left(x^2 + y^2\right) + 2\left(\frac{1-\mu}{r_1} + \frac{\mu}{r_2}\right) + \left(1-\mu\right)\mu \tag{4}$$

2.2 Hill's problem

Hill's problem is a special case of the CR3BP and is appropriate for spacecraft orbits near the secondary mass and for planetary systems with a small μ (Szebehely, 1967, Hénon, 1997, Hénon, 1969, Meyer et al., 2009). The CR3BP is characterised by the mass parameter μ, and when μ = 0 the problem reduces to the Keplerian model as viewed in a rotating system. If now we consider μ that tends to zero, it is possible to derive a simplified system of equations (Hénon, 1997, Hénon, 1969). Formulation of Hill's problem differs from the CR3BP in that the centre of the new synodic system $\bar{\xi} - \bar{\eta}$ (from now on Hill' system), is now at m_2, and m_1 acting as a perturbing body at negative infinity on the $\bar{\xi}$ axis. Figure 2 shows the geometry of the Hill's problem where ρ is the distance of the spacecraft from the Earth in the Hill' system, the non-inertial system centred at m_2. Note that, with respect to the convention adopted by Szebehely (see (Szebehely, 1967), p. 697) we retain here the convention for the direction of the reference system with the x and $\bar{\xi}$ axis in the direction m_1 to m_2, (Stramacchia, 2013). Starting with the equations of the PCR3BP in dimensionless form Eqs. (1), a translation along the x-axis is performed to centre the system at m_2:

$$\begin{aligned} \bar{\xi} &= x - 1 + \mu \\ \bar{\eta} &= y. \end{aligned}$$

This translation locates the primary body at $\bar{\xi} = -1$, $\bar{\eta} = 0$ in the Hill' system, and the secondary body at $\bar{\xi} = 0$, $\bar{\eta} = 0$. Then, by introducing a scale factor μ^α, function of the mass parameter of the planetary system under study, we can change the normalised distances ($\bar{\xi} = \mu^\alpha \xi$, $\bar{\eta} = \mu^\alpha \eta$) and the order of the gravitational force of m_2. In fact, if we set as Szebehely (Szebehely, 1967) $\alpha = 1/3$, the terms of the Coriolis force, the centrifugal force and the gravitational force of the secondary body are of the same order.

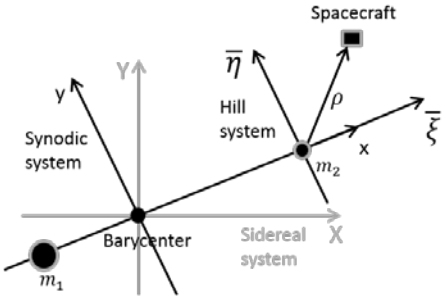

Figure 2. Geometry for the sidereal system, the synodic system and the Hill system.

Now, we can proceed with the mathematical limit process with $\mu \to 0$ (so that the distance between m_1 and m_2 goes to infinity) and, immediately, we find the equations of motion for the Hill's problem

$$\begin{cases} \ddot{\xi} - 2\dot{\eta} = 3\xi - \dfrac{\xi}{\left(\xi^2 + \eta^2\right)^{3/2}} = \dfrac{\partial \Omega_H(\xi,\eta)}{\partial \xi} \\ \ddot{\eta} + 2\dot{\xi} = -\dfrac{\eta}{\left(\xi^2 + \eta^2\right)^{3/2}} = \dfrac{\partial \Omega_H(\xi,\eta)}{\partial \eta} \end{cases}$$

with the associated pseudo-potential function

$$\Omega_H(\xi,\eta) = \frac{1}{2}\left(3\xi^2 + \frac{2}{\left(\xi^2 + \eta^2\right)^{1/2}}\right)$$

while the Jacobi integral for the Hill' system is

$$\Gamma\left(\xi,\eta,\dot{\xi},\dot{\eta}\right) = -\left(\dot{\xi}^2 + \dot{\eta}^2\right) + 3\xi^2 + \frac{2}{\left(\xi^2 + \eta^2\right)^{1/2}} \tag{5}$$

which is related to J by (Hénon, 1997)

$$J = 3 - 4\mu + \mu^2 + \mu^{2/3}\Gamma \tag{6}$$

In this model we have only two collinear equilibrium points located at $L_1 = \left[-3^{-1/3}, 0\right]$ and $L_2 = \left[+3^{-1/3}, 0\right]$, associated to the Jacobi integral for the Hill's system $\Gamma = 4.32674871$.

3 Orbit families in the PCRTBP

The work by Hénon (Hénon, 1997, Hénon, 1969) identified four typologies of simple-periodic planar orbits (i.e., crossing the ξ-axis only twice in each orbital period); these families, following Hénon's notation, are:

- Family-*f*: stable distant retrograde orbits around the second body (i.e. Distant Retrograde Orbits, DROs) (Hénon, 1997, Hénon, 1969, Xue and Junfeng, 2013, Dutt and Sharma, 2012, Demeyer and Gurfil, 2007, Lam and Whiffen, 2005);
- Family-*g*: stable/unstable distant prograde orbits around the second body with a double close approach to the second body (i.e. Distant Periodic Orbits, DPOs)[5](Hénon, 1997, Hénon, 1969, Mingotti, 2010, Mingotti et al., 2010);
- Family-*a*: unstable-retrograde orbits around the Libration point L_2 with a close approach to the second body (Demeyer and Gurfil, 2007);
- Family-*c*: unstable-retrograde orbits around the Libration point L_1 with a close approach to the second body (Demeyer and Gurfil, 2007);

3.1 Numerical computation of periodic orbits

Starting from the initial conditions found by Hénon for the Hill's problem (Hénon, 1969), see page 230, it is convenient to represent each periodic orbit with a point in the (Γ, ξ_0) plane, where ξ_0 is the abscissa of the point where the orbit crosses the ξ-axis in the positive direction, with η increasing. The symmetry of the orbit implies that, for each point in the (Γ, ξ_0) plane, we have $\eta = 0$ and $\dot{\xi} = 0$; hence, once ξ is known, $\dot{\eta}$ can be determined from Eq. (5). Of the two solutions only the one with $\dot{\eta} > 0$ must be chosen in order to cross the ξ-axis in the positive direction. The initial conditions for the periodic orbits in the Hill's dynamics by Hénon (Hénon, 1969) are here refined with a differential correction method coupled with a continuation method (Koon et al., 2011, Scott and Spencer, 2010, Thurman and Worfolk, 1996). Each orbit family is then reproduced in the PCR3BP dynamic using the same numerical procedure, which is described in Appendix A.

Figure 3 shows a map of the single-periodic orbits in the (Γ, ξ_0)-plane, taking into account the Hill's dynamics, where each periodic orbit is represented by a marker considering Hénon data (Hénon, 1969), while continuous curves represent the new numerical data found by a numerical continuation method.

[5] Family-*g* orbits are prograde orbits; for $\Gamma \to +\infty$ the orbits become very small, quasi-circular curves around the second body. They are stable if their dimension is not too large, i.e. $\Gamma > 4.5$ for the Sun – (Earth + Moon) planetary system, otherwise they become unstable.

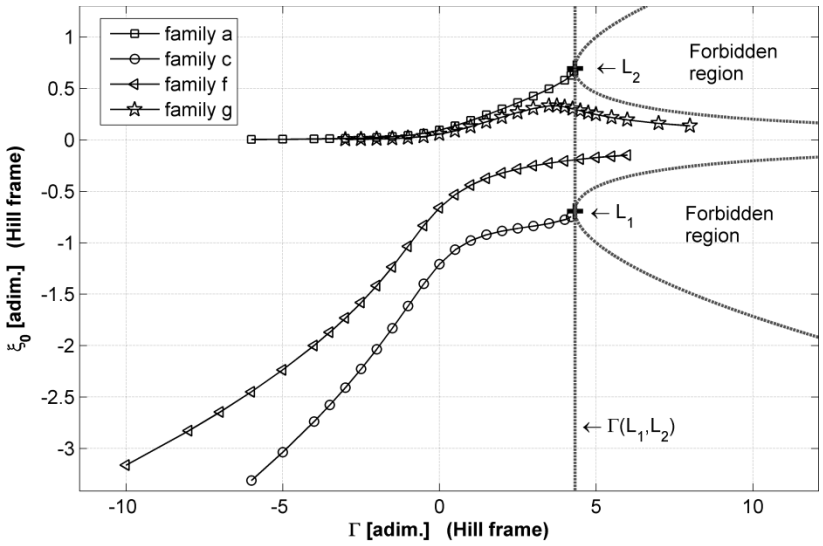

Figure 3. Map of the single-periodic orbits in the (Γ, ξ) plane considering Hill's dynamics. Dotted lines bound the forbidden regions where the velocities become imaginary, L_1 and L_2 are the Libration points, while $\Gamma(L_1, L_2)$ is the value of the Jacobi integral for the Hill's system at the Libration points.

3.2 General orbital taxonomy

Figure 4 represents the orbits of family-*f* (i), family-*g* (ii), family-*a* (iii), and family-*c* (iv), for the Sun – (Earth + Moon) PCR3BP respectively.

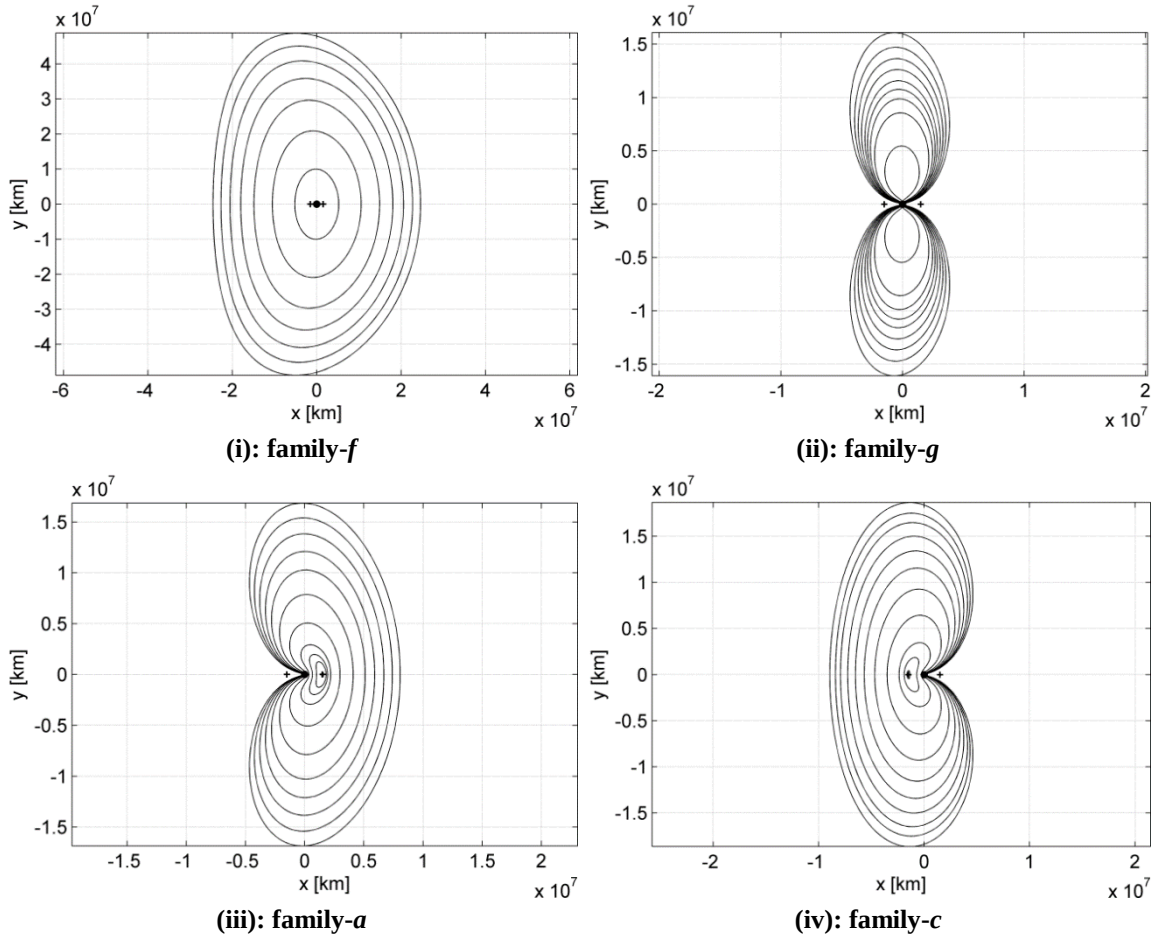

Figure 4. Simple periodic orbital families in Earth-centred synodic system. The three markers in the plot are L_1, Earth and L_2 (from left to right). (i) Family-*f*, (ii) family-*g*, (iii) family-*a* and (iv) family-*c*.

Each of these families can be extended to $\Gamma \to \pm\infty$ (families *f*, and *g*) or $\Gamma \to -\infty$ (families *a* and *c*). However, for families *a*, *c*, and *g*, the minimum distance from Earth goes to zero as this limit is approached, so the minimum distance from the Earth is limited to $r_{min} \geq 6478\,\text{km}$, which corresponds in the (Γ, ξ_0)-plane to $\xi_0 \geq 0.003$ for family-*g* and family-*a*, and to $\xi_0 \geq -4.12$ for family-*c* considering the Sun – (Earth + Moon) PCR3BP. Orbits of family-*f* with a maximum distance from Earth greater than $5 \cdot 10^7$ km will increasingly feel the gravitational effect of the other planets (e.g., Jupiter and Venus). For this reason, in the following, we will restrict our analysis to orbits reaching a maximum distance from Earth below $5 \cdot 10^7$ km, which corresponds to $2.6 \cdot 10^7$ km along the *x*-axis, or $\xi_0 \geq -12$ in the (Γ, ξ_0) plane for family-*f*. Future work will extend this family beyond this distance by implementing an *n*-body dynamics model. Set these constraints, it is possible to generate, for each family, the orbit with the highest feasible energy, presented in Table 2. It is clear that, taking into account the distance constraints, the most favourable orbit

family to obtain large distances from Earth, and consequently, good and different conditions for observation and monitoring of PHAs, is the family-*f* as some of these orbits have a characteristic dimension (i.e., minimum distance from the Earth) that is larger than the Earth-L_2 distance. Family-*f* orbits are stable, planar, and retrograde around the Earth. These characteristics of family-*f* are of some practical interest, since they mean that spacecraft can orbit at a very large distance from the second body, much further than the collinear Libration point L_1 and L_2, and, as we will see in Section 4.3, the sky-coverage performances of a space-based survey system are related to the orbital distance achievable by the spacecraft. In Section 3.3, we will discuss the orbital characteristics of family-*f*.

Table 2. Orbital values for the four families taking into account the distance constraints. (*T*: orbital period; V_{min} and V_{max}: min and max orbital velocity; r_{min} and r_{max}: min and max orbital distance to the Earth; *J*: Jacobi integral). Values in Earth-centred synodic system considering the larger orbit within each family.

Orbit family	*T* [days]	V_{min} [km/s]	V_{max} [km/s]	r_{min} [km]	r_{max} [km]	*J* [km^2/s^2]
family-*f*	365.10	5.2514	11.013	$2.6264 \cdot 10^7$	$5.2447 \cdot 10^7$	2.9689
family-*g*	494.11	1.3558	11.159	$6.5756 \cdot 10^3$	$1.8705 \cdot 10^7$	2.9980
family-*c*	499.49	1.2040	11.194	$6.5127 \cdot 10^3$	$1.6863 \cdot 10^7$	2.9984
family-*a*	669.86	0.82322	11.072	$6.6163 \cdot 10^3$	$1.6093 \cdot 10^7$	2.9993

3.3 Orbital taxonomy of family-f

This section presents the taxonomy of family-*f*, in terms of maximum and minimum orbital distance from the Earth and the orbit stability index. Table 3 (in Section 4.3.2) contains the minimum and maximum distance of the orbits from the Earth. For an orbital period of more than around 150 days, the orbit distance from the Earth is larger than the distance from L_2. The orbital period has an asymptotic behaviour towards the Earth orbital period, as the distances increase. The orbital stability index (see Appendix A for its definition) is always in the range $-2 < k < 2$, confirming the stability of the orbits (Hénon, 1997, Hénon, 1969, Koon et al., 2011, Perko, 2013). Given the numerical results for the Sun – (Earth + Moon) system in Figure 4, in Figure 5 the evolution of the family-*f* in the PCR3BP for a number of planetary systems, real and hypothetical, with mass parameter varying from the mass parameter for the Sun – (Earth + Moon) system to the mass parameter for the Earth–Moon system is studied. Each curve has a monotone decreasing behaviour, and each point on these curves represent a stable retrograde periodic orbit. This result is of some practical interest, since it corroborate the fact that retrograde spacecraft can exist at a very large distance from the second body, much further than the associated Libration points, a matter of interest in relation to asteroid detection. However, this is true only in so far as the PCR3BP is a good approximation of the planetary system considered. More precisely, starting from the refined data computed in Section 3.1, the first curve computed is that for the Sun – (Earth + Moon)

planetary system. These new initial conditions are then used as first guess in order to compute the next curve, characterised by a new larger mass parameter (i.e. $\mu = 10^{-5}$). The process is then repeated for the remaining curves. Note that, even if we are representing the periodic orbits in the PCR3BP, we prefer to keep their characterisation in the (Γ, ξ_0) plane (typical of the Hill's problem) because it allows a better comparison between different planetary systems. For each of the curve in Figure 5, the distance constraint on ξ_0 could be computed as $\xi_0 \mu^{1/3} L_{m_1-m_2} \leq L_{(x-axis)_{\max}}$, once the value of the mass parameter is associated to the correct planetary system. Therefore, the characteristic distance between the primary and secondary body $L_{m_1-m_2}$, and the maximum orbital distance reachable from the secondary body, $L_{(x-axis)_{\max}}$, can be computed. While $L_{m_1-m_2}$ is a data characteristic of a specific planetary system, the maximum orbital distance reachable can be computed considering the third-body perturbation, or more precisely the *n*-body dynamic. The maximum orbital distance reachable dictates the orbital choice within the family-*f*. For a given energy (i.e., Γ in the Hill' system), orbits with a smaller mass parameter move closer to the secondary body in the adimensional synodic system, because the ξ coordinate in the Hill' system increases in modulus as the mass parameter decrease, while orbits with a large mass parameter move away from the secondary body. In fact, reminding that $\overline{\xi} = \mu^{1/3} \xi$ and considering for example the Sun – (Earth + Moon) and the Earth – Moon systems, the $\overline{\xi}$ coordinate for the Sun – (Earth + Moon) is larger in modulus than that for the Earth – Moon system. The reason is that, if the mass parameter is small, then the region of the gravitational influence of the secondary body is also smaller in comparison to the gravitational influence of the primary, which makes the dynamical region moving closer to the secondary body for a given energy (Dutt and Sharma, 2012, Meyer et al., 2009).

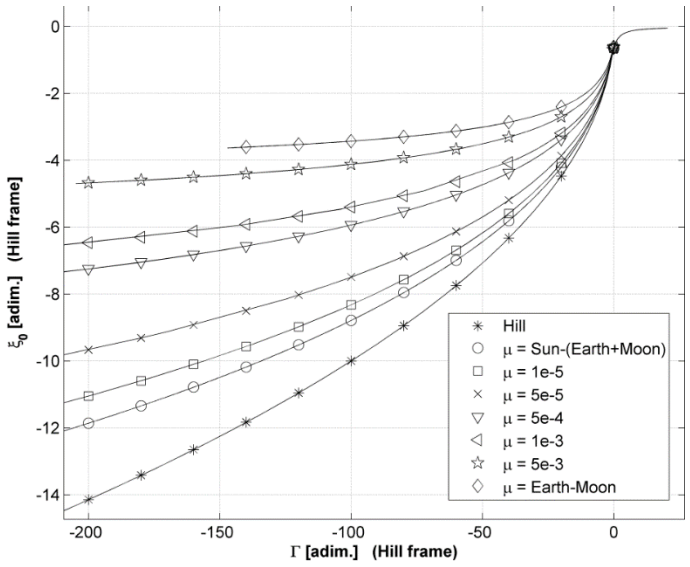

Figure 5. Evolution of the family-*f* map in the (Γ,ξ_0) plane, taking into account the PCRTBP for a number of planetary systems, actual and hypothetical, with mass parameter lying between $\mu_{Sun-(Earth+Moon)}$ and $\mu_{Earth-Moon}$. The plot does not take into account the ξ_0 distance constraints.

4 NEOs detection from distant retrograde orbits

In this section, we analyse the potentialities of DROs for asteroid and comets detection. As noted by Valsecchi et al. (Valsecchi et al., 2012), a spacecraft on one orbit of family-*f* travels around the Sun, in formation with the Earth, such that the orbit in a Sun-centred inertial system looks as a quasi-ellipse around the Sun (see Figure 6). Figure 7 shows the trend of the pseudo-semi-major axis and pseudo-eccentricity for all the orbit of family-*f* considered in this paper (see Table 3). Note that we refer to pseudo-semi-major axis and pseudo-eccentricity in stress that these two quantities are computed using the equations of the two-body problem, but considering the state vector obtained with the PCRTBP. Their trend is not constant along the orbital period, however the differences are very small (i.e., $a_{\max} - a_{\min} \approx 28803$ km and $e_{\max} - e_{\min} \approx 0.051 \cdot 10^{-3}$ for orbit *f*-4 in Table 3). As it can be seen from Figure 7, while the orbital eccentricity increases, the pseudo semi-major axis decreases and tends to 1 AU, measured in the Sun-centred inertial system, and the orbital period asymptotically converges to the Earth orbital period. Moreover, as the eccentricity increases, the orbits move further and further away from the Earth's orbit (Valsecchi et al., 2012).

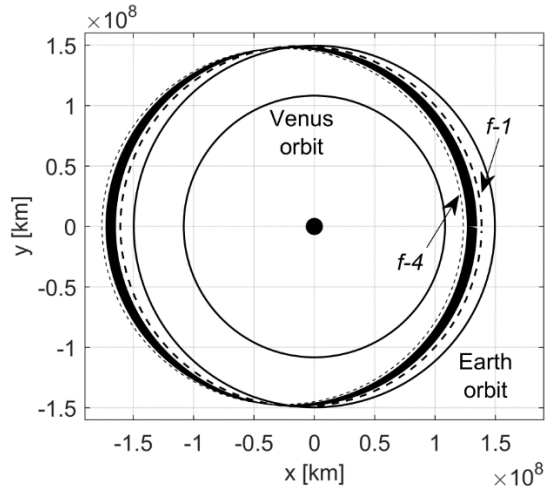

Figure 6. Family-*f* orbits in the Sun-centred sidereal system (black solid line). *f*-1 and *f*-4 orbits are in dashed lines , while the relative orbits' parameters are reported in Table 3 (Section 4.3.2). For comparison, Venus and Earth orbits are shown.

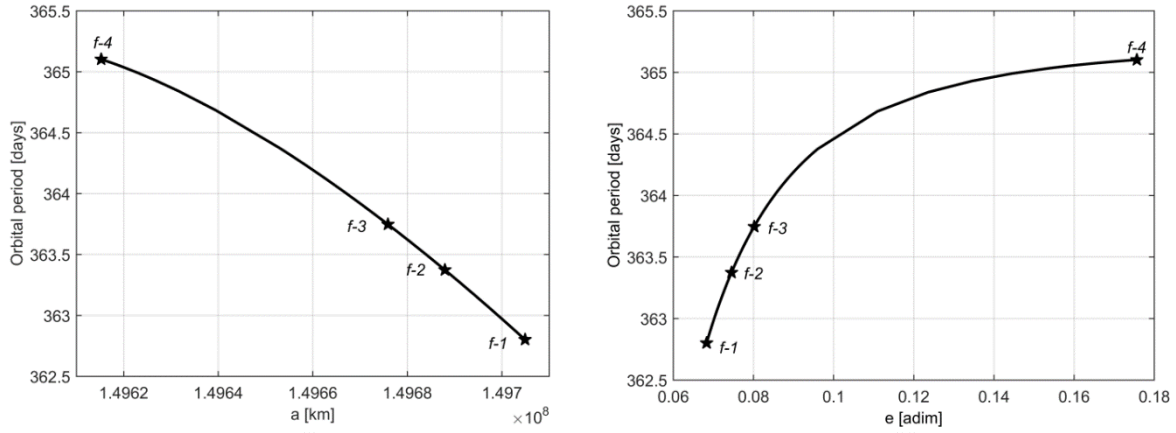

(i) **(ii)**

Figure 7. Trend of the pseudo-semi-major axis (i) and pseudo-eccentricity (ii) for family-*f* orbits in the Sun-centred sidereal system. The four star markers are for the orbits summarised in Table 3 (Section 4.3.2).

On a DRO the spacecraft travels in retrograde direction, as seen from Earth, with its minimum geocentric distance $r_{\min}$ corresponding to the inferior conjunction, and maximum geocentric distance $r_{\max}$ at quadrature (see Figure 8). The minimum and maximum geocentric distances can be approximated as function of the orbit eccentricity expressed in AU computed with respect to the Sun-centred inertial system as derived by Valsecchi (Valsecchi et al., 2012). Taking into account a four spacecraft constellation, the particular positions along the orbit *f*-3 in Table 3 are show in Figure 8. Each spacecraft of the constellation is characterised by the same orbital trend in term of distances and velocities, what change are only the initial values of distances and velocities of each spacecraft, because they start at different orbital positions. These initial positions are equally spaced in time, considering the dynamics in Eq. (1), and just for

the four spacecraft constellation they correspond to the characteristic orbital positions (i.e. inferior and superior conjunction and quadrature).

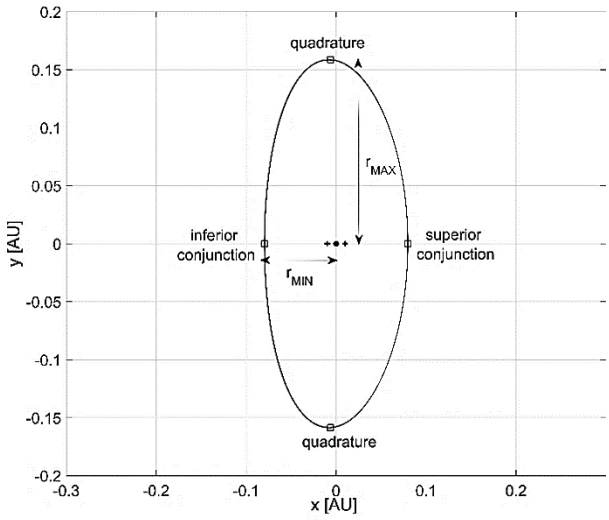

Figure 8. Spacecraft particular positions for a four spacecraft constellation on *f*-3 orbit in Table 3 (Section 4.3.2), with minimum and maximum geocentric distance at inferior conjunction and quadrature respectively. The three markers in the middle of the plot are L_1, the Earth, and L_2 from left to right respectively, while the four square markers are the spacecraft (values in Earth synodic system).

4.1 H-G astronomical model to compute asteroid size

In order to assess PHAs detection capabilities from a given orbit and to compare it with the capabilities from Earth-based detection, it is useful to compute the minimum asteroid diameter that can be observed from a given point in space, considering current telescope technologies. One of the challenges when observing asteroids is their rapid and drastic variations in magnitude. The magnitude of asteroids does not only depend on physical parameters, such as the size and the albedo, but also on its rotational state, the distances to the Sun $R_1(t)$, the observer $R_2(t)$, and the phase angle $\kappa(t)$, which is the angle between the light incident onto the observed object and the light reflected from the object (in the context of astronomical observations this is usually the angle illuminator-object-observer). The apparent magnitude or visual magnitude *V* is a measure of the object brightness as seen by an observer, adjusted to the value it would be in the absence of the atmosphere. *V* can be computed as (Binzel et al., 1989, Buchheim, 2010, Michelsen et al., 2003, Dymock, 2010).

$$V = H + 5\log_{10}\left(R_1(t)R_2(t)\right) - 2.5\log_{10}\left(\left(1-\tilde{G}\right)\Phi_1\left(\kappa(t)\right) + \tilde{G}\Phi_2\left(\kappa(t)\right)\right) \quad (7)$$

where *H* is the object absolute magnitude, a measure of the intrinsic brightness of a celestial body. *H* is defined as the apparent magnitude that the asteroid would have if it were at 1 AU from both the Sun and the observer (in our case

the observer can be at the Earth or at the spacecraft) at zero solar phase angle. $\Phi_1\left(\kappa(t)\right)$ and $\Phi_2\left(\kappa(t)\right)$ are two phase functions that describe the single and multiple scattering of the asteroid's surface (Dymock, 2010):

$$\Phi_1\left(\kappa(t)\right) = exp\left(-3.33\left(\tan\left(\frac{\kappa(t)}{2}\right)\right)^{0.63}\right)$$
$$\Phi_2\left(\kappa(t)\right) = exp\left(-1.87\left(\tan\left(\frac{\kappa(t)}{2}\right)\right)^{1.22}\right) \quad (8)$$

In Eq.(7), $R_1(t)$ and $R_2(t)$ are expressed in AU. Measurements of the asteroid's position (i.e., astrometry data) can be used to calculate the orbit of the asteroid and thus $R_1(t)$ and $R_2(t)$ at the time of the observation. The phase slope parameter $\tilde{G}$, a value between 0 and 1, describes how the asteroid brightness falls with increasing solar phase angle. In this work $\tilde{G}$ = 0.15 was considered, corresponding to a low-albedo for C-type asteroids (Luu and Jewitt, 1989, Veeder et al., 1992). The model in Eq. (7) was previously used by Sanchez and Colombo (Sanchez and Colombo, 2013) to assess the time required for detecting PHAs from an Earth and near-Earth telescope network.

Figure 9 shows the geometrical configuration for the two survey systems considered.

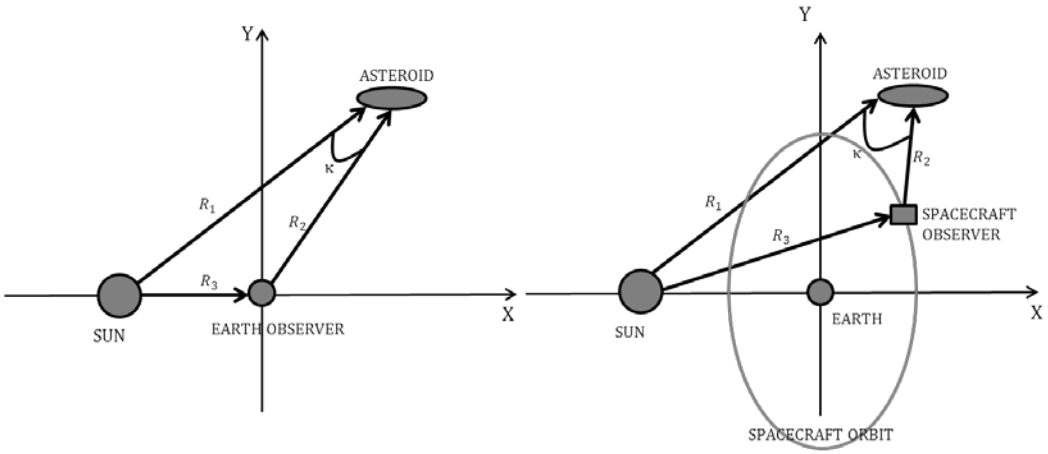

Figure 9. Geometry configuration for ground-based survey system, and space-based survey system, in the synodic system with Earth at the origin.

Eq. (7) gives the variation of the visual magnitude with time, as the asteroid moves around the Sun. If we assume a limiting visual magnitude $V_{\lim}$ below which asteroids can be detected, the limiting absolute magnitude $H_{\lim}$ at each time can be obtained from Eq. (7). As the asteroid moves around the Sun, the smallest asteroid size $D_{\min}$ that can be detected from a given orbit (i.e., the orbit of the Earth for ground-based survey or the spacecraft's orbit for

space-based survey) as a function of time can be obtained as in (Sanchez and Colombo, 2013, Michelsen, 2004, Perna et al., 2013, Werner et al., 2002).

$$D_{\min} = \frac{1}{\sqrt{p_v}} \cdot 1329 \cdot 10^{-H_{lim}/5} \quad [\text{km}] \tag{9}$$

where p_v is the asteroid's albedo. Care is needed when evaluating the size of the smallest asteroids (i.e. sub-kilometre size), as the actual albedo p_v of these objects is currently not known. However in the present analysis $p_v = 0.154$ is considered as an average value for the asteroid's albedo (Veeder et al., 1992). The apparent magnitude *V* in Eq.(7) takes into account a full sky coverage, but in reality the sky coverage of an asteroid survey by ground telescopes is limited to the night side of the Earth, and to relatively large solar elongation (i.e., the angle between $R_2(t)$ and $R_3(t)$ in Figure 9). In fact, the asteroids cannot be observed from ground if their direction is close to the direction of the Sun. Eq. (7), via the phase functions $\Phi_1(t)$ and $\Phi_2(t)$, has the effect of increasing the apparent magnitude and so decreasing the brightness of the asteroid. If the phase angle $\kappa(t)$ increases and approaches 180°, the visual magnitude *V* increases towards infinity and so this decreases the brightness of the asteroid. In the following, Eq. (9) is used to assess the capabilities of an Earth-based or a space-based PHAs detection system. Depending on the definition of the observer, the phase angle $\kappa(t)$ is the Sun-asteroid-Earth or Sun-asteroid-spacecraft angle; $R_2(t)$ is the distance in AU of the asteroid to the Earth, for ground-based survey systems, or to the spacecraft, for space-based survey systems. $V_{lim} = 23$ was set as the limiting visual magnitude for space-based survey as in (Sanchez and Colombo, 2013), while $V_{lim} = 24$ as the limiting visual magnitude for ground-based survey, which corresponds to the capability of the Pan-STARRS, the Panoramic Survey Telescope & Rapid Response System developed at the University of Hawaii's Institute for Astronomy (Vereš et al., 2009, Stokes et al., 2002, Todd et al., 2011, Todd et al., 2012).

4.2 Ground-based survey systems

The observing capabilities of a ground-based survey system are determined by the atmospheric conditions. The duty cycle for these survey systems is limited by daylight and weather. They have access to a bit less than 2 sr of the total sky at any time, and furthermore, much of this area of the sky is at zenith angles and so unfavourable due to atmospheric effects. The part of the sky observable further narrows during winter nights (Stokes, 2003). On the contrary, space-based survey systems are not limited by these effects and have a greater duty cycle. These space systems can have access to more than 3 sr. This depends on the Sun exclusion zone of the spacecraft sensor and so

they allow surveying a larger portion of the sky. The Sun exclusion zone is approximately 40 degrees half angle from the sunlight direction (Stokes, 2003). In the following, we assume also for the ground telescope the same exclusion zone of the space systems. In this way, we adopt conservative conditions and we can compare the observational potentialities of the two different survey systems. Using Eqs. (7) and (9) the minimum observable diameter as function of the distance can be computed; this produces a family of "heart-shaped" curves (Stokes et al., 2002, Sanchez and Colombo, 2013). These curves represent the minimum asteroid size that can be observed if we have a precise geometrical configuration between the Earth (i.e., observer), the Sun and the asteroids (for a ground-based system), or between the spacecraft (i.e., observer), the Sun and the asteroids (for a space-based system). As previously done in (Sanchez and Colombo, 2013), a search grid in the Earth-centred synodic system is considered with boundaries of ± 1 AU, with Earth at the origin of this reference frame and the Sun at -1 AU. Set a 1000 point on the grid (x, y), which represents a generic PHA, the vector position of the asteroid respect to the Sun in dimensionless units can be defined as:

$$\mathbf{R}_1(t) = \begin{bmatrix} x+1 \\ y \end{bmatrix}$$

The vector position of the asteroid respect to the Earth based observer is:

$$\mathbf{R}_{2,\,\text{Earth}}(t) = \begin{bmatrix} x \\ y \end{bmatrix}$$

The phase angle $\kappa(t)$ is then computed from the Carnot theorem as:

$$\cos\kappa(t) = \left(\left\|\mathbf{R}_1(t)\right\|^2 + \left\|\mathbf{R}_{2,\,\text{Earth}}(t)\right\|^2 - \left\|\mathbf{R}_3(t)\right\|^2 \right) \Big/ \left(2\left\|\mathbf{R}_1(t)\right\| \left\|\mathbf{R}_{2,\,\text{Earth}}(t)\right\| \right) \tag{10}$$

where $\mathbf{R}_3(t)$ is the vector position of the observer respect to the Sun (where the observer is the Earth telescope in this case, see Figure 9).

For each point of the grid, the minimum detectable size diameter from Earth $D_{\text{min, Earth}}(x, y)$ is computed from Eq. (9). Figure 10 represents the capabilities of current NEOs discovery search programs in terms of minimum diameter of the asteroid to be detected: BISEI with $V_{\text{lim}} = 19.0$, SPACEWATCH with $V_{\text{lim}} = 21.7$, and Pan-STARRS with $V_{\text{lim}} = 24.0$ (Stokes et al., 2002). The contour plot in Figure 10 shows that, as expected, a ground telescope with a greater V_{lim} is able to observe a wider portion of sky for a given diameter of the asteroid ($\bar{d}_{\text{min}} = 80$ m in this case);

therefore, the probability to detect an asteroid grows considerably. However, some boundaries need to be defined beyond which no asteroid can be observed. Indeed, as per spacecraft-based survey systems, the Earth-based systems have a Sun exclusion zone of about 40 degrees half angle from the Sun–Earth line. For this reason, if the asteroid is within such region, the detectable diameter is set to zero.

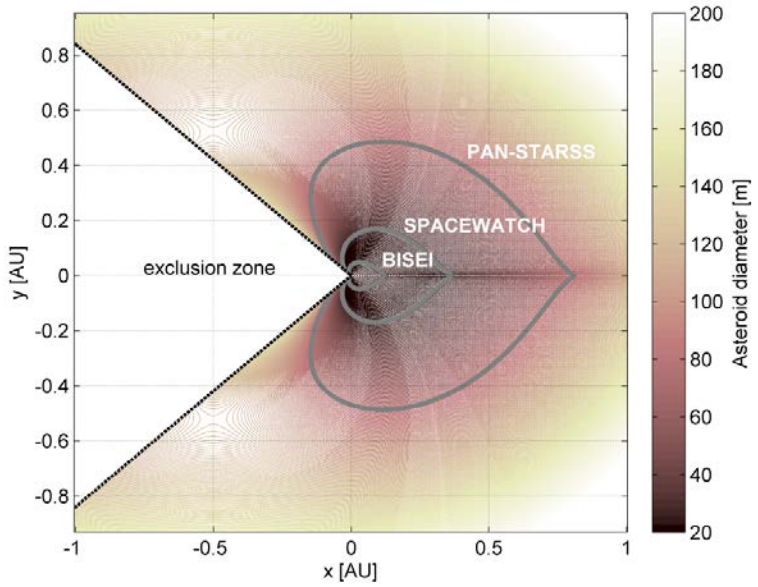

Figure 10. Comparison of three current NEOs search programs for detection of asteroids with minimum diameter D_{min} of 80 m (Earth centred synodic system).

4.2.1 Numerical computation of $A_{coverage,\ Earth}$

Now, fixing the minimum asteroid size we want to detect, $\bar{d}_{\min}$, the capabilities of an Earth-based survey system can be measured by computing the area of the region of space which is enclosed by the level curve at $\bar{d}_{\min}$ defined as the sky coverage area $A_{\text{coverage-Earth}}$ measured in AU^2. First, we define a grid in (x, y) to represent the generic position of a virtual asteroid at any distance from the Earth. Each point of the (x, y) grid represents a virtual asteroid; for each point of the grid (i.e., a given distance from the Earth) the minimum diameter that can be detected at that distance is computed based on Eq. (9) and it is stored in a matrix $\mathbf{D}_{\text{min, coverage-Earth}}$. Then, given the required target diameter $\bar{d}_{\min}$, the boundaries of the coverage areas are defined as the contour line $\bar{\mathbf{d}}_{\text{min, coverage-Earth}}$ associated to $\bar{d}_{\min}$. $\bar{\mathbf{d}}_{\text{min, coverage-Earth}}$ is numerically found computing the isolines of matrix $\mathbf{D}_{\text{min, coverage-Earth}}$ using the contour function implemented in

Matlab. Then, the area inside the polygons defined by the contour line matrix $\bar{\mathbf{d}}_{\mathbf{min,\ coverage-Earth}}$ is computed to get $A_{\text{coverage-Earth}}$ in AU^2.

Figure 11 shows the $A_{\text{coverage-Earth}}$ as function of the minimum asteroid diameter that can be detected, considering V_{lim} values for four different ground-based survey systems. Each of these V_{lim} values is used in Eq. (7) in order to compute the new values of H_{lim}, therefore using Eq. (9) the new surfaces matrix $\mathbf{D}_{\mathbf{min,\ coverage-Earth}}\big|_{H_{\text{lim}}}$ can be computed, along with $\bar{\mathbf{d}}_{\mathbf{min,\ coverage-Earth}}\big|_{H_{\text{lim}}}$. For a fixed asteroid diameter, $A_{\text{coverage-Earth}}$ increases as the V_{lim} increases, and this trend grows more for large asteroid diameters. However, ground-based survey systems fail in the case of PHAs incoming from the Sun direction, because the exclusion zone cannot be monitored.

The fundamental steps for the numerical computation of $A_{\text{coverage-Earth}}$ are summarised in Algorithm 1 in Appendix B.

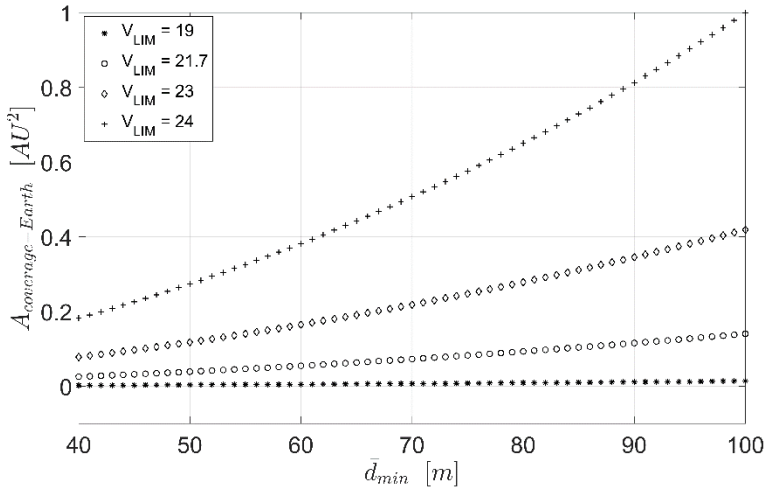

Figure 11. Evolution of the $A_{\text{coverage-Earth}}$ taking into account the V_{lim} values for four different ground-based survey systems.

4.3 Space-based survey systems

In this section, the orbital dynamics in Eqs. (1) is coupled with the *H-G* astronomical model in Eqs. (7) and (9), to investigate the advantages of a space-based system over a ground-based system in terms of sky coverage area $A_{\text{coverage-space}}$ measured in AU^2. As said, the attractive feature of the family-*f* orbits is the large distance that they reach from Earth. Therefore, from these orbits, spacecraft carrying a telescope can potentially monitor a larger portion of

the space surrounding the Earth, and detecting PHAs with better figures of merit, in comparison to the ground-based system. The expression of $\mathbf{R}_1(t)$ still holds, while the vector position of the asteroid respect to the space observer, based at $\left[x_{s/c}(t) \quad y_{s/c}(t)\right]^T$ to Earth, is

$$\mathbf{R}_{2,\,\text{space}}(t) = \begin{bmatrix} x - x_{s/c}(t) \\ y - y_{s/c}(t) \end{bmatrix}$$

while the vector position of the observer respect to the Sun is

$$\mathbf{R}_{3,\,\text{space}}(t) = \begin{bmatrix} x_{Sun} - x_{s/c}(t) \\ y_{Sun} - y_{s/c}(t) \end{bmatrix}$$

from which $\kappa(t)$ can be again computed from the Carnot theorem.

As an initial consistency analysis, we can compare the minimum asteroid diameter that can be observed with just one spacecraft at inferior conjunction (i.e., spacecraft in between the Sun and the Earth) for several *f*-orbits, considering a predefined circular warning zone constraint with a radius R_{wz} of 0.1 AU from the centre of the Earth (i.e., black circle in Figure 12). We here set the requirement that the asteroid is visible in the warning zone , considering asteroids with a geocentric mean velocity equal to $V_{geo,\,\text{PHA}}$ =15 km/s (Belton, 2004, Valsecchi et al., 2012) and consequently an 11.5-days warning time prior to a close approach to the Earth from the warning zone, computed in first analysis as

$$t_w = R_{wz} / V_{geo,\,\text{PHA}} \tag{11}$$

To ensure that the asteroid is visible from space also in the case it is coming from the direction away from the Sun (i.e., from the +*x*-axis), the minimum asteroid diameter was computed at *x* equal to the radius of the warning zone, identifying the warning distance. In this case, the vector positions, used to compute the minimum asteroid diameter are $\mathbf{R}_1 = \begin{bmatrix} x_{Sun} + R_{wz} \\ 0 \end{bmatrix}$, $\mathbf{R}_{2,\,\text{space}} = \begin{bmatrix} R_{wz} - x_{s/c} \\ 0 \end{bmatrix}$, and $\mathbf{R}_{3,\,\text{space}} = \begin{bmatrix} x_{Sun} - x_{s/c} \\ y_{Sun} \end{bmatrix}$, therefore $\kappa = 0$ because $\mathbf{R}_1$ and $\mathbf{R}_{2,\,\text{space}}$ are aligned. In this case, only $\mathbf{R}_{2,\,\text{space}}$ is changing, because we are considering spacecraft at the inferior conjunction of different orbits (i.e. $x_{s/c}$ changes), and asteroids placed at the warning zone, along the +*x*-axis (i.e., asteroid coordinates equal to $x = R_{wz}$, $y = 0$). The phase functions are equal to one, and the asteroid absolute magnitude at the warning zone is $H_{\text{lim},wz} = V_{\text{lim}} - 5\log_{10}\left(\left\|\mathbf{R}_1\right\|\left\|\mathbf{R}_{2,\,\text{space}}\right\|\right)$. The minimum asteroid diameter detectable at the warning

zone, $\bar{d}_{\text{min, } wz}$ is then computed with Eq. (9), using $H_{\text{lim},wz}$ (and reported in Table 3). Therefore, the surface matrices for both the survey systems, computed with Algorithm 1 and 2 in Appendix B, are used to extract the two contour line matrix associated to $\bar{d}_{\text{min, } wz}$. This information is then used to compute the heart-shaped curves for both the survey-systems, and the results are illustrated in Figure 12.

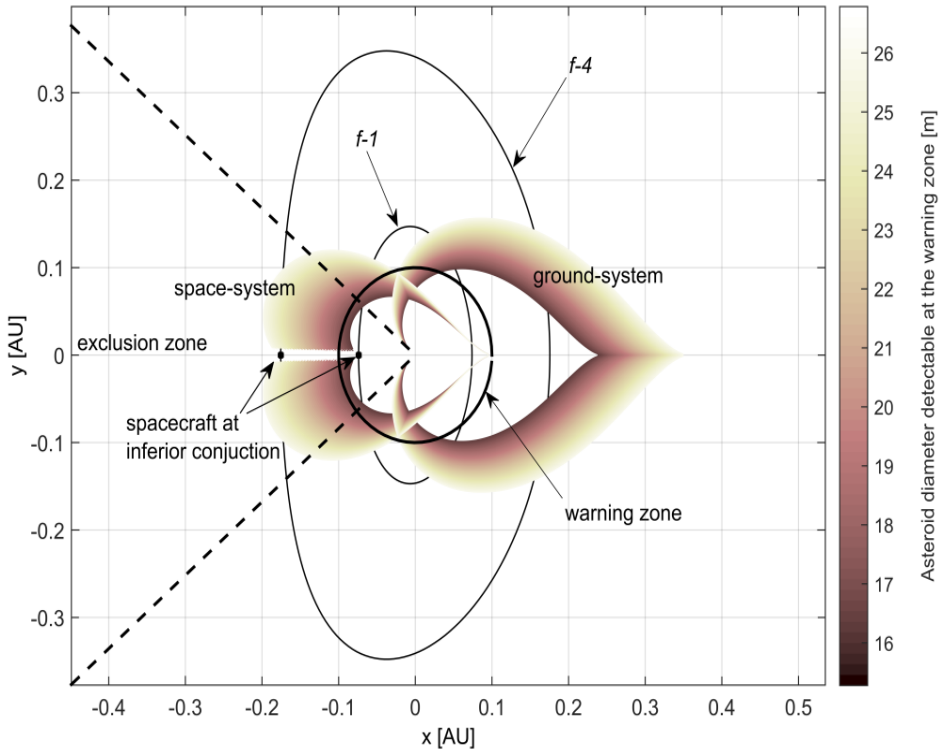

Figure 12. Graphical comparison of Earth and space-based survey systems, considering the minimum asteroid diameter detectable with 11.5-day warning time (Sun at -1 AU along *x*-axis). The space-based survey systems is characterised by only one spacecraft at the inferior conjunction. The two black circle markers represent the spacecraft for orbits *f*-1 and *f*-4 in Table 3 (values in Earth synodic system).

In this figure, for clarity, only the *f*-1 and *f*-2 orbits of family-*f* in Table 3 are shown, together with the corresponding spacecraft position at the inferior conjunction. For each orbit contained within the family-*f*, the minimum diameter of the asteroid detectable at the warning distance was computed as explained above, and graphically compared with the coverage area of the ground-based telescope, considering the same $\bar{d}_{\text{min, } wz}$. As an initial consistency check, ground-based survey systems offer higher values of $A_{\text{coverage-Earth}}$, in comparison to a single space telescope, characterised by lower values of $A_{\text{coverage-space}}$. However, Earth systems prove to be unable to detect asteroid incoming from the Sun-Earth direction. Consistent with intuition, we can note in Figure 12 that spacecraft at inferior conjunction assure a

maximum coverage inside the exclusion zone, in comparison to the others orbital positions, and this coverage improves considering orbits with high energy. Moreover, since we desire at the same time a good coverage of the space surrounding the Earth, and an adequate warning time prior the asteroid close approach with the Earth atmosphere, a potential solution is to match the two survey systems, assuring at least the warning zone coverage. We can argue that the size and position respect to Earth and Sun, of each space heart-shaped curve, should have a strong impact on warning time and space coverage inside the exclusion zone.

Nevertheless, we must consider that the minimum detectable diameter and coverage area from space-based observation depends on the instantaneous position of the spacecraft on its orbit. For this reason, the temporal evolution of the space-based coverage area will be now computed, by creating the spatial envelope of a multi-spacecraft constellation for different time instant from 0 to T (i.e., the orbit period). The spatial envelope, $A_{\text{coverage-space}}$, covered by the spacecraft in the constellation, is a function of the constellation size $N_{s/c}$, and the spacecraft orbital positions. The contour line matrix associated to each spatial envelope, is then used together with the exclusion zone constraint, to compute $A_{\text{exclusion zone, space}}$ measured in AU^2.

4.3.1 Numerical computation of $A_{coverage,\ space}$ and $A_{exclusion\ zone,\ space}$

The only difference respect to Earth detection model is that this time the surface matrix $\mathbf{D}_{\text{min, coverage-space}}$ is computed for each spacecraft in the constellation. Therefore, $N_{s/c}$ contour line matrices $\bar{\mathbf{d}}_{\text{min, coverage-space}}$ are constructed, considering the desired value of the asteroid diameter $\bar{d}_{\min}$, and the geometrical envelope is searched. The feasibility of this envelope is strictly related to the orbital size (i.e., the value of $r_{\min}$), to the size of the constellation (i.e., the value of $N_{s/c}$) and to the spacecraft geometrical configurations along the orbit. When the feasibility is satisfied, it means that the envelope does not shows blind region (see Figure 13 and Figure 14).

The spacecraft configuration is a function of time, because the spacecraft are moving and therefore their relative positions are changing. The rate of changing of the relative positions is high for a constellation with low number of spacecraft. $N_{s/c}$ has also a great impact on the orbital trend of $A_{\text{exclusion zone, space}}$ and less on $A_{\text{coverage-space}}$. Moreover, taking into account the symmetrical property of family-*f*, the spacecraft configurations obtained within the first half-period can be obtained in reverse order in the second half of the orbit period. Hence, the evolution of the spatial envelope will be symmetric with respect to the orbital period. This symmetry can also be exploited to reduce the cost for

computing $\mathbf{D}_{\text{min, coverage-space}}$. The fundamental steps for the numerical computation of $A_{\text{coverage-space}}$ and $A_{\text{exclusion zone, space}}$ are summarised in Algorithm 2 in Appendix B.

4.3.2 Family-f orbits selection

In Table 3 we have summarised the data for five characteristics orbits used throughout this work. More precisely *f*-1 and *f*-4 represent the boundary orbits of the entire family-*f* analysed in Figure 6 and Figure 7. These characteristic orbits are optimised taking into account the full envelope feasibility used to compute $A_{\text{coverage-space}}$, and $A_{\text{exclusion zone, space}}$ for a space-based survey system. In other words, each of these orbits were selected through an optimisation process, considering a predefined constellation size and using, as a first guess the relative value of $\bar{d}_{\text{min, wz}}$ in Table 3. The optimisation process first checks the feasibility of the full envelope for the initial configuration (i.e., unique envelope); if feasible, it moves to the second spacecraft configuration and checks again. In the case of an unfeasible full envelope, the algorithm freezes the current spacecraft configuration and increases the asteroid diameter by $\Delta\bar{d}$. Therefore, checks for the full envelope, if feasible move to the new spacecraft configuration, otherwise freezes again and increase the asteroid diameter as before. This process is repeated until the spacecraft configurations are exhausted. The number of spacecraft configuration is equal to 360 in each orbital period, and $\bar{d}_{\text{min, full}}$ represents the minimum asteroid diameter detectable in each spacecraft configuration with a feasible full envelope.

Table 3. Family-*f* orbits analysed (*f*-1 and *f*-4 are the first and last orbit of the family, *f*-2 and *f*-0 are the orbits used for Chelyabinsk detection in Section 5, *f*-3 is the orbit used for the constellation analysis in Section 4.3.3). (*T*: orbital period; r_{min} and r_{max}: min and max distance spacecraft-Earth in the synodic system; *e*: pseudo-eccentricity; *a*: pseudo-semi-major axis; *J*: Jacobi integral; $\bar{d}_{\text{min, wz}}$: minimum asteroid diameter observable from the orbit in order to cover the warning zone from the inferior conjunction position; $\bar{d}_{\text{min, full}}$: minimum asteroid diameter observable from the orbit in order to have a full envelope for each spacecraft configuration, considering a 4-spacecraft constellation size).

Orbit ID	*T* [days]	r_{min} [AU]	r_{max} [AU]	*e* [-]	*a* [AU]	*J* [-]	$\bar{d}_{\text{min, wz}}$ [m]	$\bar{d}_{\text{min, full}}$ [m]
f-0	357.54048	0.04586458	0.09017932	0.04731	1.0015176	2.9978839	13	17
f-1	362.80133	0.06762312	0.13450745	0.06829	1.0007154	2.9954105	15	26
f-2	363.37367	0.07395897	0.14729024	0.07452	1.0006020	2.9945112	16	28
f-3	363.74734	0.07969226	0.15883077	0.08017	1.0005215	2.9936277	17	45
f-4	365.10272	0.17556456	0.35058794	0.17566	1.0001160	2.9689252	25	68

4.3.3 Impact of orbit size, orbital dynamics and constellation size

As noted in Figure 12, the orbit size has a very strong impact on the coverage area inside the exclusion zone, even if considering one spacecraft positioned at the optimal orbital configuration (i.e., the inferior conjunction). These preliminary results show that the $A_{\text{exclusion zone, space}}$ increases as $r_{\min}$ increases, and this is consistent with the choice of family-*f*, because this family in the only one that increase the distances from Earth along both the axis. Therefore, the orbits belonging to this family are the most favourable in term of distances from Earth, and consequently they offer good conditions for observation and monitoring of PHAs.

However, the results so far have been obtained disregarding the orbital dynamics of the spacecraft. In order to study the impact of the spacecraft dynamics, a spacecraft constellation is now introduced. More precisely, this constellation can be interpreted as a group of $N_{s/c}$ formation-flying spacecraft, moving in identical *f*-orbit in a trailing formation. Each spacecraft follows the previous one separated by a specific time interval ΔT, to view a portion of sky surrounding the Earth at different times. ΔT is a fraction of the orbital period computed as $\Delta T = T/N_{s/c}$. Similarly to the Earth-based system, the coverage area of the space based system, $A_{\text{coverage, space}}$, can be computed.

Figure 13 clarifies the definition of the spatial envelope (grey area + dark grey area) and shows the gained monitoring area within the exclusion zone, $A_{\text{exclusion zone, space}}$, for space-based systems (dark grey area). The orbital dynamics has some impact on the geometry of the space envelope, and therefore on the value of $A_{\text{coverage-space}}$. Looking at the space coverage inside the exclusion zone, for the initial configuration, one spacecraft is inside the exclusion zone at the inferior conjunction, see Figure 13 (i), while for the other configuration three spacecraft are outside the exclusion zone, while the fourth is on the boundary of the exclusion zone, see Figure 13 (ii). The value of $A_{\text{exclusion zone, space}}$ seem to be strictly related to the geometry of the spacecraft position and therefore to the orbital dynamics, and this is clearly illustrated in Figure 13 where the geometry of the coverage area within the exclusion zone is symmetric for the initial configuration, and distorted in the other case. In the Introduction of this paper, we highlighted a correlation between the geometry of the coverage area within the exclusion zone and the asteroid's trajectory, and their influence over the warning time. Asteroids performing close encounters with the Earth within the exclusion zone cannot be tracked from Earth. Therefore, a spacecraft constellation prove to be useful, and in what follow the impact of orbit size, orbital dynamic, and constellation size is investigated, considering an asteroid diameter of 45 m, a 4-spacecraft constellation, and for the orbital dynamic orbit *f*-1 and *f*-4 in Table 3 are used.

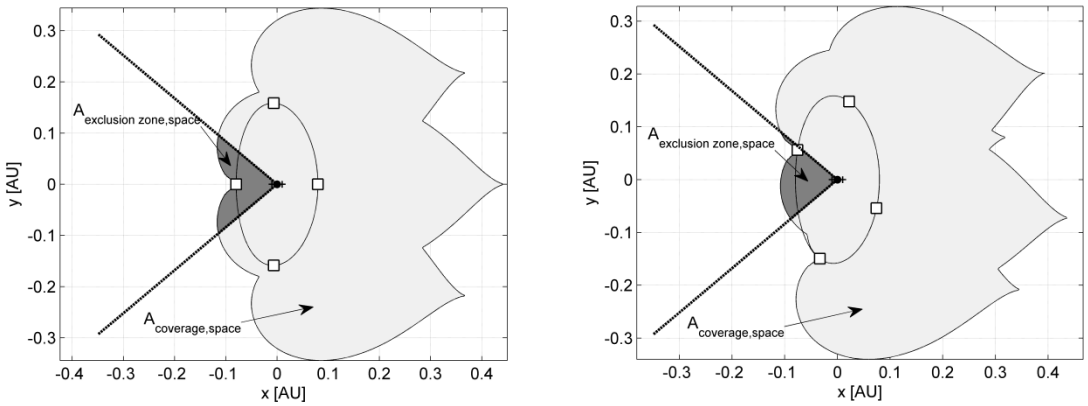

(i) **(ii)**

Figure 13. $A_{\text{coverage, space}}$ **and** $A_{\text{exclusion zone, space}}$ **for space-based system: (i) 4-spacecraft constellation considering the initial configuration; (ii) 4-spacecraft constellation after 20 days. Constellation analysed considering the *f*-3 orbit in Table 3, with** $\overline{d}_{\min} = 45\,\text{m}$**.**

Figure 14(i) shows the spatial envelope from *f*-1 orbit, for a detection of minimum asteroid diameter of 45 m. Two different configurations of a 4-spacecraft constellation are shown for two times along the natural evolution when the worse (dashed line) and best (solid line) coverage area are obtained. The spacecraft positions for the maximum and minimum coverage are also shown with triangle and square markers, respectively. Note that, the selection of the minimum asteroid diameter to be detected drives the choice of the orbit size (i.e., the value of $r_{\min}$). For a constellation, this choice is more challenging, because the envelope feasibility has to be taken into account. The envelope feasibility must be guaranteed for each instant of time throughout the orbital dynamics. Figure 14(ii) shows the spatial envelope obtained at the initial configuration on the *f*-1 orbit (grey dashed line) and *f*-4 orbit (black solid line) considering a minimum asteroid diameter of 45 m and a 4-spacecraft constellation. As we can see the spatial envelope is symmetric respect to the *x*-axis in both cases, but the topology is completely different. In the first case, the *f*-1 orbit is a better choice as it allows a continuous coverage (i.e., full spatial envelope). In the second case, the coverage from the *f*-4 orbit presents some "blind" zones (i.e., the spatial envelope is disconnected). In this case, only two spacecraft form a connected coverage area, while the area covered by the other two members of the constellation is disconnected. This may be improved by increasing the number of spacecraft in the constellation or by increasing $V_{\lim}$ (i.e., increasing the performance of the telescopes). It is indeed clear that a correlation exists between the full spatial envelope for each time instant, the size of the constellation and the orbit amplitude, therefore a trade-off of these parameters is essential.

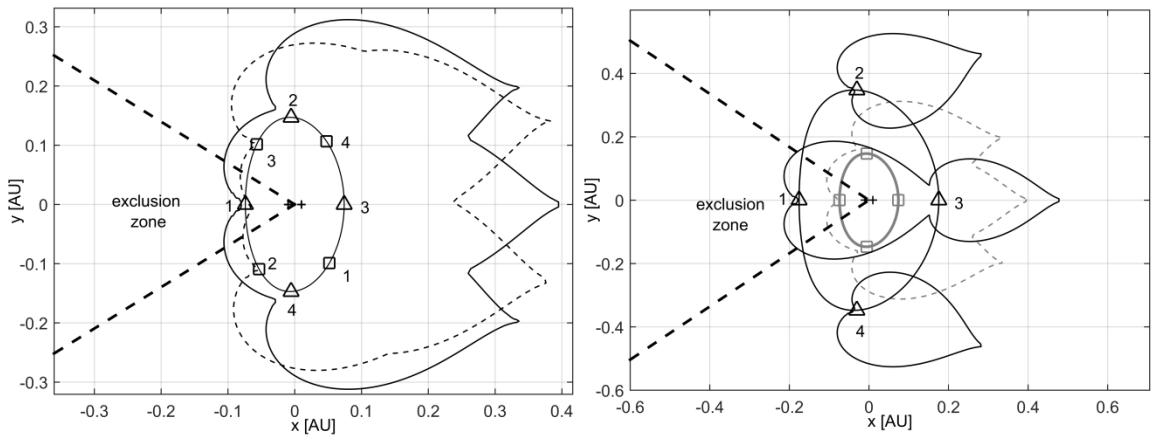

(i) **(ii)**

Figure 14. Spatial envelope for a 4-spacecraft constellation. (i) Evolution of the spatial envelope in time for the *f*-1 orbit in Table 3, together with the spacecraft positions (each number represents a different spacecraft). Two different instant of time are considered, the best configuration (solid line, triangle markers), and the worse configuration (dashed line, square markers). (ii) Spatial envelope at the initial configuration on *f*-1 (grey dashed line) and *f*-4 (solid black line) orbits in Table 3, considering the same spacecraft constellation. The numbers indicate the spacecraft order, and is the same in both the orbits.

Now, considering different constellation sizes (i.e., composed by 3 up to 12 spacecraft), we can compute the orbital trend of total coverage area $A_{\text{coverage-space}}$ and the orbital trend of the coverage area within the exclusion zone $A_{\text{exclusion zone, space}}$. The latter region is the main advantage of space-based observation versus Earth-based observation. A minimum diameter of 45 m is chosen in order to obtain a full envelope for each constellation and spacecraft configuration, considering the *f*-3 orbital dynamics.

Figure 15(i) shows the evolution of the global coverage area $A_{\text{coverage-space}}$, while Figure 15(ii) shows the area within the exclusion zone $A_{\text{exclusion zone, space}}$, measured in AU^2 for different constellation sizes. The evolution for both $A_{\text{coverage-space}}$, and $A_{\text{exclusion zone, space}}$ is characterised by a sinusoidal trend. This is due to the orbital dynamics and therefore on the evolution of the geometrical configuration of the spacecraft on the orbit. As an initial consistency check, we note that $A_{\text{coverage-space}}$ improves as the constellation size increases, and the amplitude of the sinusoidal trend decrease. The amplitude trend is consistent with intuition as the distortion of the orbital spacecraft configuration decreases as the constellation size increases; therefore, the difference between the worse configuration and the best configuration decreases. In the case of 3-spacecraft constellation, the trend of $A_{\text{coverage-space}}$ is sinusoidal with an amplitude modulation. These oscillations in time are probably due to the fact that the spacecraft are so distant from each other on the orbit, that consequently, their relative configuration geometry gets more distorted during the orbit evolution. We can argue

that this distortion could have a very strong impact on the warning time, because the probability to detect an asteroid in the case of a poor spacecraft geometry configuration increases.

The orbital trend of the maximum of $A_{\text{exclusion zone, space}}$ considering the different constellation sizes is similar, while the minimum increases with the number of spacecraft in the constellation. Regarding this trend it appears that the maximum value of $A_{\text{exclusion zone, space}}$ is less affected by the orbital dynamics and constellation size. However, as the constellation size increase, the number of times in which $A_{\text{exclusion zone, space}}$ is maximised in one orbital period increases. If we compare the trend obtained with a 3 and 6 spacecraft constellation, we can see that in the first case $A_{\text{exclusion zone, space}}$ reaches its maximum value four times, while a 6-spacecraft constellation seven times. Therefore, the probability to detect an asteroid within the exclusion zone with a good spacecraft geometry configuration (i.e., good warning time) increases as the constellation size increases. Moreover, it should be stressed that the warning time is also influenced by how the $A_{\text{exclusion zone, space}}$ is spread inside the exclusion zone.

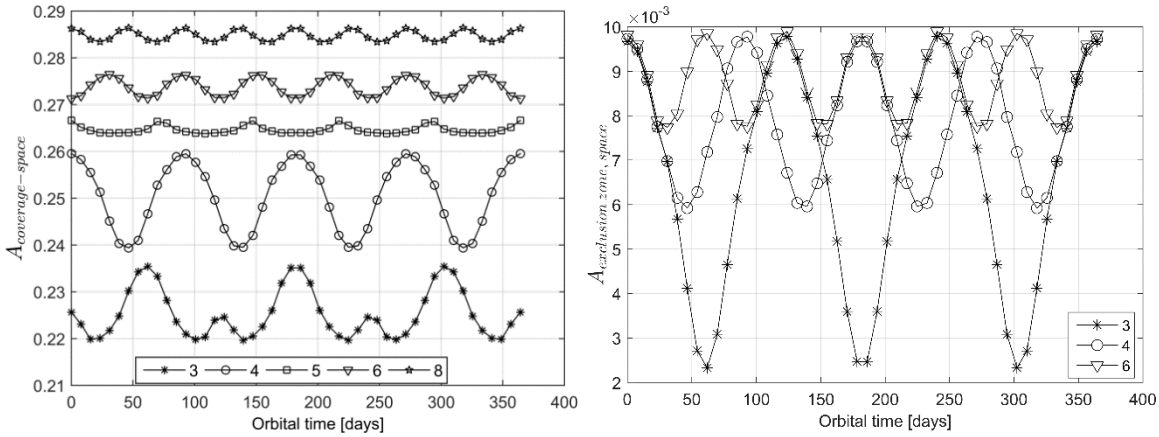

(i) **(ii)**

Figure 15 (i) Orbital trend of $A_{\text{coverage-space}}$, where five different constellation are considered (3, 4, 5, 6, and 8-spacecraft constellation); (ii) orbital trend of $A_{\text{exclusion zone, space}}$ where only three different constellation are considered for better visibility (3, 4, and 6-spacecraft constellation). In both figures the orbital dynamics is based on *f*-3 orbit in Table 3, and $\bar{d}_{\min} = 45$ m.

In Figure 16, we show the extreme values of $A_{\text{coverage-space}}$ and $A_{\text{exclusion zone, space}}$ as a function of the constellation size. In the case of $A_{\text{coverage-space}}$, as the constellation size increases, the minimum and maximum values tend asymptotically to the mean value. The extreme values of $A_{\text{exclusion zone, space}}$ have a different trend; here the minimum and mean values

tend asymptotically to the maximum value, reinforcing the fact that the constellation size has a strong impact on the min value of $A_{\text{exclusion zone, space}}$ and a less noticeable effect on the maximum value.

The evolution of $A_{\text{exclusion zone, space}}$ and $A_{\text{coverage-space}}$ can be extended to a higher number of spaceraft in the constellation to show their asymptotic behaviour, disregarding for now both the feasibility and cost of the overall mission (see Figure 17). In this case, only the initial orbital spacecraft configuration is considered, because as stated before, the impact of the orbital dynamics is less noticeable as the constellation size increase. For the orbit considered, $A_{\text{coverage-space}}$ has the major increment for 3 up to 15-spacecraft constellation, while $A_{\text{exclusion zone, space}}$ has the major increment for 3 up to 21-spacecraft constellation. As the constellation size increase, the detection area within the exclusion zone became less distorted, approaching a triangular shape, as we can see in the small plot inside Figure 17, while the space envelope area become more and more smooth.

In general, increasing the size of the constellation gives a more robust PHA detection system especially in terms of coverage of the exclusion zone, which should be always guaranteed. However, it should be stressed that various factors may influence the numerical results found within these plots; namely, the parameters used in the *H*-*G* astronomical model (i.e., the phase slope parameter and the asteroid's albedo). Moreover, even if these results are strongly correlated with the selection of the orbit amplitude and asteroid diameter, we can argue that the qualitative trend would be similar and just the quantitative trend would change in the case of different $r_{\min}$ and $\bar{d}_{\min}$.

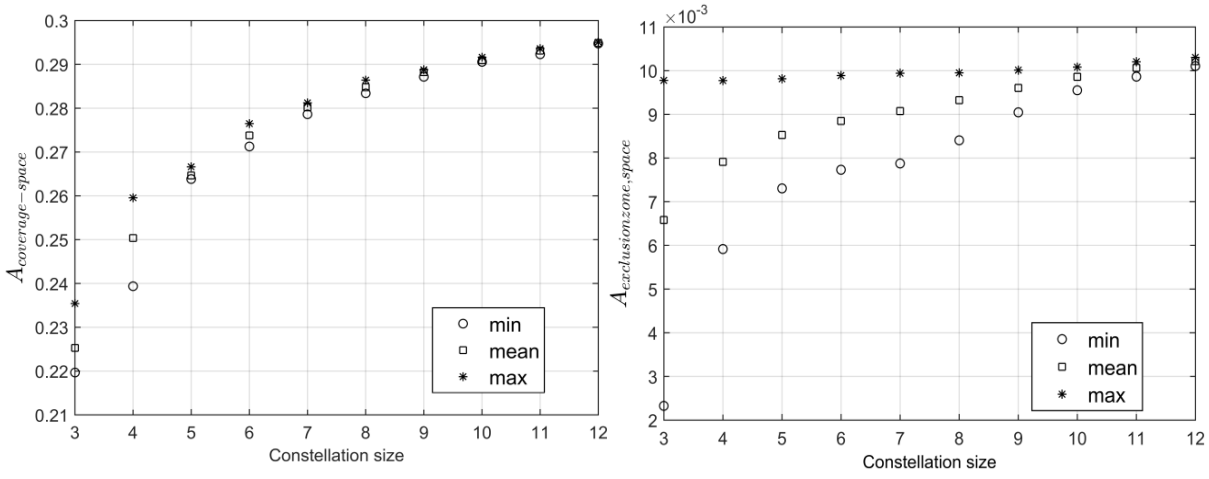

Figure 16. (i) Max, mean and min values for $A_{\text{coverage-space}}$; (ii) max, mean and min values for $A_{\text{exclusion zone, space}}$. Constellation analysed considering *f*-3 orbit in Table 3 with $\bar{d}_{\min} = 45$ m.

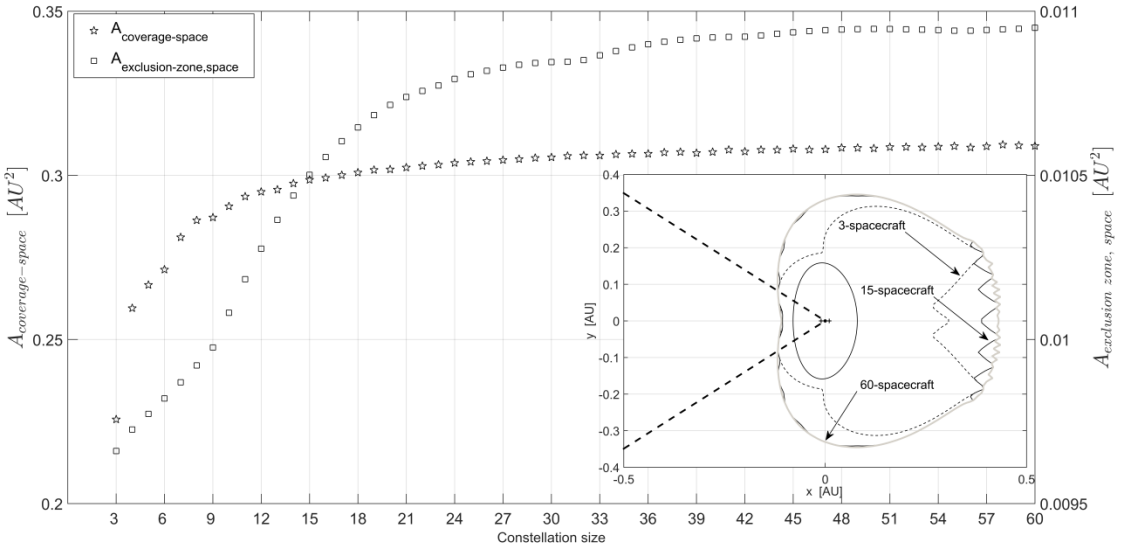

Figure 17. Asymptotic behaviour of $A_{\text{coverage-space}}$ and $A_{\text{exclusion zone, space}}$ considering the initial spacecraft configuration. The small plot in the right bottom corner is a graphical comparison of 3 constellations size from which we can see the shape evolution of $A_{\text{coverage-space}}$ and $A_{\text{exclusion zone, space}}$. The constellation have been analysed considering *f*-3 orbit in Table 3 with $\bar{d}_{\min} = 45$ m.

5 Application to real scenario

Finally, in order to take into account a real asteroid trajectory, in the following as an example, we consider the case of the Chelyabinsk meteoroid. On 15 February 2013, a small asteroid entered Earth's atmosphere over Russia with an estimated speed of 18 km/s, an estimated initial mass of 11,000 tonnes and measuring approximately 17 to 30 meters across (Andronikov et al., 2014). The object exploded in an airburst over Chelyabinsk at a height of about 15 to 25 km with the generation of a bright flash, small fragmentary meteorites and a powerful shock wave. The Chelyabinsk meteor is the largest known object to have entered the Earth's atmosphere since the 1908 Tunguska event (Zuluaga and Ferrin, 2013, Andronikov et al., 2014). The object was not detected before atmospheric entry, because it came from the wrong direction for ground-based observations. In the following, we will study the potential of a space-based survey system exploiting the dynamics of DROs, to detect the trajectory of Chelyabinsk meteor. Table 4 summarises the orbital parameters of first determination of the orbit of the Chelyabinsk meteor (Zuluaga and Ferrin, 2013).

We can compute the warning time considering the intersection between the asteroid trajectory and the space coverage envelope. More precisely, the asteroid dynamics (orbital elements in Table 4) is simulated backward in time for a time span period of 100 days from the impact day. At the beginning of the simulation, the spacecraft constellation

starts at the nominal configuration, and the space envelope is computed with one-day step and is searched in order to find the intersection with the asteroid trajectory. The orbits chosen for the simulation assure the feasibility of the space envelope for each spacecraft configuration. Therefore, from the intersection position, the time at the intersection is computed and used to evaluate the best and worse detection in term of days.

In order to show the impact of the orbit amplitude and asteroid diameter over the warning time, two different cases has been analysed. In the first case, the Chelyabinsk diameter was set to $\bar{d}_{\min} \geq 30$ m, while in the second case $\bar{d}_{\min} \geq 17$ m. To have a connected spatial envelope along the orbital period, the *f*-2 orbit in Table 3 was selected for $\bar{d}_{\min} \geq 30$ m. In this way, Chelyabinsk trajectory could be monitored, and the most favourable conditions happening when the space envelop geometry intersects the Chelyabinsk trajectory as much as possible away from the Earth. For $\bar{d}_{\min} \geq 17$ m a smaller orbit than *f*-1 in Table 3 was selected, in order to guarantee a connected spatial envelope along the entire orbital period, namely *f*-0 in Table 3. Figure 18 shows the orbital trend of $A_{\text{exclusion zone, space}}$ and warning time considering both the cases described earlier (i.e. two orbit amplitude and two asteroid diameters). As we can see, despite some irregularities, the warning time trend follows the $A_{\text{exclusion zone, space}}$ trend, disregarding the orbit amplitude and the value of $\bar{d}_{\min}$. These irregularities are primarily due to the distribution of $A_{\text{exclusion zone, space}}$ over the *x*-*y* plane, respect to the asteroid's trajectory. More precisely, even if the $A_{\text{exclusion zone, space}}$ is increasing, for some spacecraft orbital configuration this area is spread inside the exclusion zone but far away from the incoming asteroid trajectory. This could jeopardise the detection capability in terms of warning time, because the intersection between the asteroid trajectory and the space envelope move to the Earth proximity. A potential solution able to minimise these irregularities, is increasing the constellation size, however at higher mission cost.

Figure 19 illustrates the heart-shape curve for the ground-based survey system and the best and worse coverage for space-based survey system considering two different $\bar{d}_{\min}$ as before. The black circles show the position of the asteroid every five days along the orbital trajectory. As a first check, we can see that with a ground telescope it is impossible to detect the asteroid, because its orbital trajectory lie within the exclusion zone. Conversely, with a space-based system it is possible to detect the asteroid with a 15.52 days warning time, for the best spacecraft configuration, and with a 3.67 days, for the worst spacecraft configuration, considering an estimated minimum diameter of $\bar{d}_{\min} \geq 30$ m. In the case of $\bar{d}_{\min} \geq 17$ m, the warning time decrease to 8.62 days for the best spacecraft configuration,

and 36 minutes for the worse. Therefore, in the case of $\bar{d}_{\min} \geq 17$ m a 4-spacecraft constellation gives a marginal warning time for the worse spacecraft configuration. In order to increase the warning time, a potential solution is to increase the size of the constellation. Figure 20 illustrates the orbital trend of $A_{\text{exclusion zone, space}}$ and warning time, using a 5-spacecraft constellation and *f*-0 orbit. As a consistency check, we can see that the warning time for the best configuration is less sensible to the change in the constellation size, while the warning time for the worse spacecraft configuration improve noticeably, increasing from 36 minutes to 4.52 days. This improvement is related to the increment in the minimum value of $A_{\text{exclusion zone, space}}$ and to the fact that a 5-spacecraft constellation give a less distorted coverage area within the exclusion zone, in comparison to a 4-spacecraft constellation.

In conclusion, a small constellation of four spacecraft properly spaced in time along the same DRO, could be quite effective for asteroid detection, like Chelyabinsk, with a reasonable warning time, in the case of $\bar{d}_{\min} \geq 30$ m. Otherwise, for asteroid diameter around 20 m, a large constellation prove to be quite effective in order to increase the warning time of the worse spacecraft configuration, as per the Chelyabinsk meteoroid. This would give the possibility to take protective measures against small meteoroid approaching from the line of sight to the Sun. Furthermore, such DROs constellation could be effective to complete the catalogue of NEOs down to diameter smaller than 1 km.

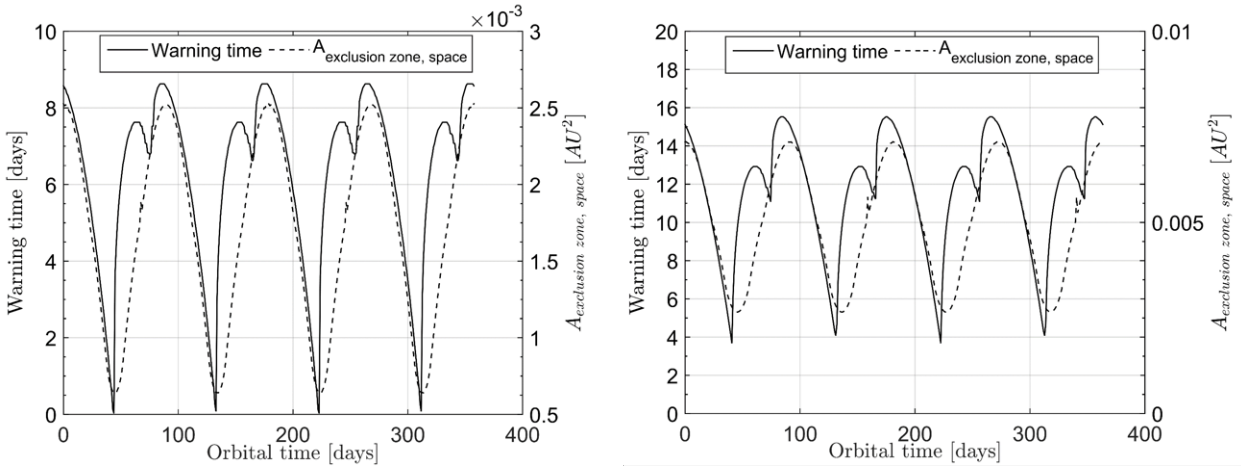

Figure 18. (i) $A_{\text{exclusion zone, space}}$ **and warning time orbital trend considering *f*-0 orbit and** $\bar{d}_{\min} \geq 17$ m**; (ii)** $A_{\text{exclusion zone, space}}$ **and warning time orbital trend considering *f*-2 orbit and** $\bar{d}_{\min} \geq 30$ m**. In both cases a 4-spacecraft constellation is used.**

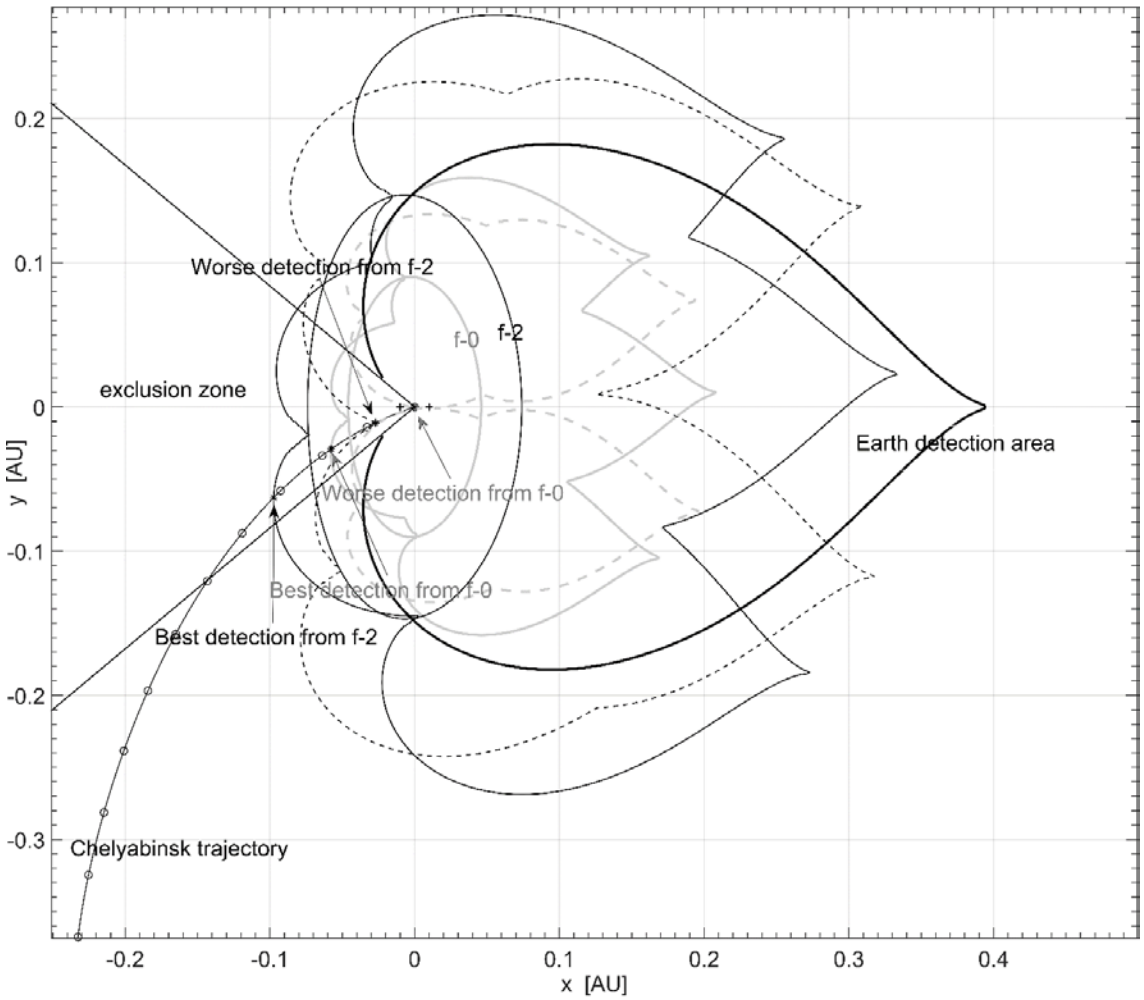

Figure 19. Representation of Chelyabinsk detection from *f*-0 and *f*-2 orbit for a 4-spacecraft constellation, considering $\overline{d}_{\min} \geq 17$ m and $\overline{d}_{\min} \geq 30$ m respectively. Earth detection area is $A_{\text{coverage-Earth}}$ for ground telescope. The black circle markers indicate the Chelyabinsk position along its trajectory every 5 days. The warning time computation is based on the intersection between the asteroid trajectory and the space envelope, which is strictly related to the size of the constellation and the spacecraft configuration (this intersection is indicated with the black asterisk markers). The four warning times are, best detection from *f*-2: 15.52 days, worse detection from *f*-2: 3.67 days, best detection from *f*-0: 8.62 days, worse detection from *f*-0: 36 minutes.

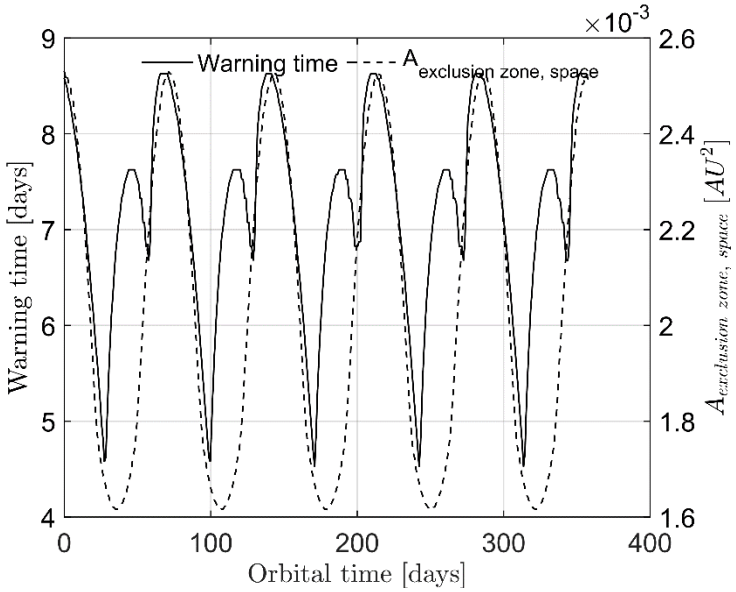

Figure 20. $A_{\text{exclusion zone, space}}$ **and warning time orbital trend considering *f*-0 orbit and** $\bar{d}_{\min} \geq 17$ m**, for a 5-spacecraft constellation. The warning times are, best detection from *f*-0: 8.63 days, worse detection from *f*-0: 4.52 days.**

Table 4. Chelyabinsk orbit data.

	Symbol (units)	min value	max value	mean value
Semi-major axis	a [AU]	1.40	2.21	1.69
Eccentricity	e [ ]	0.37	0.65	0.51
Inclination	i [°]	0.03	6.98	3.30
Longitude of ascending node	Ω	326.50	331.87	326.51
Argument of periapsis	ω	116.06	125.25	120.75
Perihelion distance	r_p [AU]	0.77	0.88	0.82
Aphelion distance	r_a [AU]	1.93	3.64	2.55

6 Conclusions

This paper proposes a concept for the space-based monitoring of PHAs from retrograde distant periodic orbits in the Sun – (Earth + Moon) system. Starting from initial conditions in Hill's problem, family of simple-periodic orbits are built in the Planar Circular Restricted Three Body Problem and their characterisation is performed according to the maximum and minimum distance they reach from the Earth. Distant Retrograde Orbits in the Sun – (Earth + Moon) systems are selected as they ensure increasing the warning time with respect to conventional Earth-based observation. Indeed the increase of coverage area and gained visibility in the Earth exclusion zone are demonstrated. Based on the analysis performed, a small constellation of four spacecraft properly spaced in time along the same DRO, could be

quite effective at detecting asteroids with a reasonable warning time. In the case of Chelyabinsk, the numerical results show that, with a space-based system composed of a 4-spacecraft constellation, it is possible to detect the asteroid with a 15.52 days warning time for the best spacecraft configuration, and with a 3.67 days for the worst spacecraft configuration (considering the capabilities of *H-G* model, $\bar{d}_{\min} \geq 30$ m and space telescopes with a limiting visual magnitude as 23). Moreover, in the case of the lower estimation diameter $\bar{d}_{\min} \geq 17$ m, the results are less encouraging, with 8.62 days and 36 minutes, for the best and worse spacecraft configuration, respectively. A potential solution in order to improve the worse warning time, has been the use of a 5-spacecraft constellation, able to increase the worse warning time from 36 minutes to 4.52 days, rather than the approximately two minutes interval time between the flash and the shock wave arrival on the Earth, in the case of Chelyabinsk impact. In future, it will be possible have telescopes with a higher $V_{\lim}$ and consequently the figure of merit used to measure the space-based detection capabilities will improve and also for a given DRO it will be possible to detect objects with a smaller diameter or for a given diameter gain higher warning time. Although we believe that such DRO constellation could be effective to complete the catalogue of NEOs down to diameter smaller than 1 km, and could be employed in space weather applications to improve the warning time of solar storms, it still has a long way to go for practical applications. Additional follow-up work is required in the near future, such as the extension to three-dimensional orbits and optimisation of their injection parameters in the Sun – (Earth + Moon) planetary system should be investigated. Furthermore, such studies should be examined in a high-fidelity model, based on an *n*-body dynamic coupled with a Station-keeping control, needed for long-term missions. The method proposed would allow for a quick and hopefully accurate first-guess choice of the baseline orbit and warning time evaluation, considering a predefined asteroid diameter, which can undoubtedly considered a very important computational tool.

Appendix A. Numerical computation of periodic orbits

Starting from the initial conditions refined from (Hénon, 1969), the new initial state vector for each orbit is computed in the Sun – (Earth + Moon) PCR3BP, considering this time a finite mass parameter μ. The differential correction method coupled with a continuation method on the orbit amplitude (i.e., energy) is used to build a complete map of periodic orbits in the (Γ, ξ_0) plane, for a specific mass parameter (Koon et al., 2011, Scott and Spencer, 2010, Thurman and Worfolk, 1996). Considering the PCR3BP, the numerical algorithm used in the differential correction

method, adjust the *y*-velocity, v_y in Eq. (1), of the periodic orbit, starting from the initial condition given by Hénon data. This initial condition is integrated until the next *x*-axis crossing, where the $\dot{x}$ value may not be zero, or in general less than a predefined tolerance, e.g. $toll = 10^{-8}$. The state transition matrix after one half-orbital period, $\Phi\left(T_{half}, 0\right)$, is used to adjust v_y, by $\delta \dot{y}_0 \approx \left(\Phi_{34} - \frac{\dot{x}\left(T_{half}\right)}{\dot{y}\left(T_{half}\right)} \Phi_{24} \right)^{-1} \dot{x}\left(T_{half}\right)$, with Φ_{ij} the *i*-*j* component of the state transition matrix, in order to cancel out $\dot{x}\left(T_{half}\right)$. This process converges to $\left|\dot{x}\left(T_{half}\right)\right| < toll$ within a few iterations typically. The state transition matrix is computed solving a linear, non-autonomous system of differential equations in 16 dimensions. These equations are called the first variational equations, and can be solved simultaneously with the equations of motion (i.e. of the PCRTBP, or Hill's model). The resulting 20 dimensional initial value problem is

$$\dot{\mathbf{X}} = f(\mathbf{X})$$
$$\dot{\mathbf{\Phi}}(\mathbf{X}, t) = \left[\frac{\partial f(\mathbf{X})}{\partial \mathbf{X}} \right] \mathbf{\Phi}(\mathbf{X}, t)$$

with initial conditions $\mathbf{X}(0) = \mathbf{X}_0$, $\mathbf{\Phi}(\mathbf{X}, 0) = \mathbf{I}$, where $\mathbf{X}$ is the state vector, $\left[\partial f(\mathbf{X}) / \partial \mathbf{X}\right]$ is the Jacobian matrix, and $\mathbf{I}$ is an (4×4) identity matrix. The solution of the state transition matrix computed at a time equal to the orbital period, T, is defined as monodromy matrix, $\mathbf{M} = \left(\partial \Phi(\mathbf{X}, t) / \partial \mathbf{X} \right)\Big|_{t=T}$. The stability of a periodic orbit is typically deduced from $\mathbf{M}$, which can be decomposed in four eigenvalues λ_i with $i = 1, ..., 4$ and their associated eigenvectors (Perko, 2013, Koon et al., 2011). Two of the eigenvalues, λ_1, λ_2 are equal to unity due to the periodicity, while the other two, λ_3, λ_4 may be real, complex, or imaginary. Due to the symplectic properties of the state transition matrix (i.e. the equations of motion are an autonomous Hamiltonian system), they appear as reciprocal pairs, hence $\lambda_3 = 1/\lambda_4$, and from the Lyapunov stability, a periodic orbit that exhibits stability is characterised by a pair of complex or imaginary eigenvalues, with a stability index, k, between $k = -2$ and $k = 2$. The stability index can be defined by $k = tr(\mathbf{M}) - 2$, or by $k = \lambda_3 + \lambda_4$. Note that the differential correction method described above is used for both the Hill's and PCR3BP dynamics.

The numerical continuation method is used to compute orbit of arbitrary large amplitude, to generate a family of orbits that reaches the desired energy level. Starting from two small nearby periodic orbit initial conditions, namely

$\mathbf{X}_0^{(1)} = \begin{bmatrix} x_0^{(1)} & 0 & 0 & \dot{y}_0^{(1)} \end{bmatrix}^T$ and $\mathbf{X}_0^{(2)} = \begin{bmatrix} x_0^{(2)} & 0 & 0 & \dot{y}_0^{(2)} \end{bmatrix}^T$, correct to within the tolerance $toll$, and computed with the differential correction procedure described above, an initial guess for $\mathbf{X}_0^{(3)}$ can be extrapolated via

$$\begin{aligned} \mathbf{X}_{0,g}^{(3)} &= \mathbf{X}_0^{(2)} + \boldsymbol{\Delta} \\ &= \begin{bmatrix} x_0^{(2)} + \Delta x_0 & 0 & 0 & \dot{y}_0^{(2)} + \Delta \dot{y}_0 \end{bmatrix}^T \\ &= \begin{bmatrix} x_{0,g}^{(3)} & 0 & 0 & \dot{y}_{0,g}^{(3)} \end{bmatrix}^T \end{aligned}$$

where $\boldsymbol{\Delta} = \mathbf{X}_0^{(2)} - \mathbf{X}_0^{(1)}$ and subscript g indicate first guess. Keeping $x_{0,g}^{(3)}$ fixed, the continuation method uses the differential correction to compute an accurate solution $\mathbf{X}_0^{(3)}$ from the initial guess $\mathbf{X}_{0,g}^{(3)}$ and repeats the process until a family of periodic orbits is obtained.

Appendix B. Algorithm for computation of sky coverage area

Algorithm 1 Earth detection model

Inputs:

1) *H-G* astronomical model parameters, p_v, $V_{\lim}$, $\tilde{G}$, and asteroid diameter $\bar{d}_{\min}$ for which $A_{\text{coverage-Earth}}$ need to be computed.
2) Lower and upper boundaries $x^l \le x \le x^u$, $y^l \le y \le y^u$ for the 2-dimensional asteroid grid in AU, and number of points in the grid, (e.g. $N_{grid} = 1000$). The boundary values can be chosen taking into account the maximum asteroid diameter allowed in the simulation (e.g., $-1 \le x \le 1$, $-1 \le y \le 1$ for asteroid diameters below 200 m),
3) Half angle for the triangle exclusion zone constraint centred at the origin of the Earth synodic system (i.e., the same half angle has been used for both the detection models, which is 40 degrees).
4) Reference system (i.e., in both the detection model, Earth-based and space-based, the Earth synodic system is used, with the Earth at the origin and the Sun at coordinates $x_{Sun} = -1$ and $y_{Sun} = 0$).

Outputs: The surface matrix $\mathbf{D}_{\text{min, coverage–Earth}}$, the contour line matrix $\bar{\mathbf{d}}_{\text{min, coverage-Earth}}$ and $A_{\text{coverage-Earth}}$.

Step 1 – Compute the asteroid grid. Considering the lower and upper boundaries, and N_{grid}, compute a square grid with dimensions $N_{grid} \times N_{grid}$. Each point in this grid represents the coordinates of a virtual asteroid.

Step 2 – For loop.

For j = 1:1: $N_{grid}{}^2$ select the asteroid coordinates (x, y) and perform the following steps.

Step 3 – Evaluate the geometry of the system. Compute the vectors $\mathbf{R}_1$, $\mathbf{R}_{2,\text{ Earth}}$, $\mathbf{R}_{3,\text{ Earth}}$, the angle κ between $\mathbf{R}_1$ and $\mathbf{R}_{2,\text{ Earth}}$ (in this detection model $\mathbf{R}_{3,\text{ Earth}}$ does not change and its modulus is equal to one).

Step 4 – Evaluate the *H-G* astronomical model Eqs. (7), and (8). Compute the phase functions Φ_1, Φ_2, and $H_{\lim}$.

Step 5 – Evaluate Eq. (9) and apply the exclusion zone constraint. Evaluate Eq. (9), change the dimension of $D_{\min}$ from kilometres to meters, and verify the solution feasibility. More precisely, if the exclusion zone constraint is satisfied store $D_{\min}$ in matrix $\mathbf{D}_{\text{min, coverage–Earth}}$, otherwise set $\mathbf{D}_{\text{min, coverage–Earth}}$ as NaN.

End.

Step 6 – Evaluate $A_{\text{coverage-Earth}}$. Once the matrix $\mathbf{D}_{\text{min, coverage-Earth}}$ is computed, extract the coordinates of the contour line associated to the asteroid with diameter $\bar{d}_{\min}$. These coordinates are collected in matrix $\bar{\mathbf{d}}_{\text{min, coverage–Earth}}$, and after a reordering procedure of the coordinates, a polygon is constructed and the associated area in AU^2 is the value of $A_{\text{coverage-Earth}}$.

Algorithm 2 Space constellation detection model

Inputs:

1) *H-G* astronomical model parameters, p_v, $V_{\lim}$, $\tilde{G}$, and the asteroid diameter $\bar{d}_{\min}$ for which $A_{\text{coverage-space}}$ need to be computed.
2) Lower and upper boundaries $x^l \le x \le x^u$, $y^l \le y \le y^u$ for the 2-dimensional asteroid grid in AU, and number of points in the grid, (e.g. $N_{grid} = 1000$). The boundary values can be chosen taking into account the maximum asteroid diameter allowed in the simulation (e.g., $-1 \le x \le 1$, $-1 \le y \le 1$ for asteroid diameters below 200 m), the orbital size (i.e., the value of $r_{\min}$), and the constellation size (i.e., the value of $N_{s/c}$).
3) Half angle for the triangle exclusion zone constraint centred at the origin of the Earth synodic system (i.e., the same half angle has been used for both the detection models, which is 40 degrees).
4) Reference system (i.e., in both the detection model, Earth-based and space-based systems, the Earth synodic system has been used, with the Earth at the origin and the Sun at coordinates $x_{Sun} = -1$ and $y_{Sun} = 0$).
5) Number of spacecraft in the constellation, $N_{s/c}$, number of envelopes along the orbital period, N_{envelope}.

Outputs: The surface matrix $\mathbf{D}_{\text{min, coverage-space}}$ with dimensions $N_{grid} \times N_{grid} \times N_{s/c}$, the contour line matrix $\bar{\mathbf{d}}_{\text{min, coverage-space}}$, $A_{\text{coverage-space}}$, and $A_{\text{exclusion zone, space}}$.

Step 1 – **Select an orbit within family-*f*.**
Step 2 – Compute the asteroid grid. Considering the lower and upper boundaries, and N_{grid}, compute a square grid with dimensions $N_{grid} \times N_{grid}$. Each point in this grid represents the coordinates of a virtual asteroid.
Step 3 – Setup envelope. Considering $N_{s/c}$, and N_{envelope} the interval time between each envelope is computed, and is used to compute the spacecraft configuration.
Step 4 – For loop

for j_{envelope} = 1:1:N_{envelope}, compute the spacecraft positions (i.e. geometry of the constellation).
for $j_{\text{spacecraft}}$ = 1:1:$N_{s/c}$
for j_{grid} = 1:1: N_{grid}^2, select the asteroid coordinates (x, y) and perform the following steps

Step 5 – Evaluate the geometry of the system. Compute the vectors $\mathbf{R}_1$, $\mathbf{R}_{2,\text{ space}}$, $\mathbf{R}_{3,\text{ space}}$, the angle κ between $\mathbf{R}_1$ and $\mathbf{R}_{2,\text{ space}}$, the angle α between $\mathbf{R}_1$ and $\mathbf{R}_{3,\text{ space}}$.
Step 6 – Evaluate the geometry in the correct system of reference. Computation of the Sun and asteroid coordinates in the new reference system centred at the spacecraft position, and aligned with the Sun-spacecraft direction. The spacecraft position is used for the translation, while the angle α is used for the plane rotation.
Step 7 – **Evaluate the *H-G* astronomical model Eqs. (7), and (8).** Compute the phase functions Φ_1, Φ_2, and $H_{\lim}$.
Step 8 – **Evaluate Eq. (9) and apply the exclusion zone constraint.** Evaluate Eq. (9), change the dimension of $D_{\min}$ from kilometres to meters, and verify the solution feasibility. More precisely, if the exclusion zone constraint is satisfied store $D_{\min}$ in matrix $\mathbf{D}_{\text{min, coverage-space}}$, otherwise set $\mathbf{D}_{\text{min, coverage-space}}$ as NaN.

end

end

Step 9 – Evaluate the envelope feasibility. Once the matrix $\mathbf{D}_{\text{min, coverage-space}}$ is computed for all the asteroids in the grid and for all the spacecraft in the constellation, it is searched in order to extract the coordinates of the contour line associated to the asteroid with diameter $\bar{d}_{\min}$. After a reordering procedure of the coordinates, $N_{s/c}$ polygons are constructed, and then the algorithm checks for the envelope feasibility, computing the number of envelope , N_e, considering the intersection between $N_{s/c}$ polygons.

if $N_e = 1$

these coordinates are collected in matrix $\bar{\mathbf{d}}_{\text{min, coverage-space}}$, and $A_{\text{coverage-space}}$, $A_{\text{exclusion zone, space}}$ are computed.

In the case of $A_{\text{exclusion zone, space}}$, the intersection between $\bar{\mathbf{d}}_{\text{min, coverage-space}}$ and the triangle exclusion zone is computed, and a new polygon is obtained. The area of this polygon is $A_{\text{exclusion zone, space}}$.

else

the algorithm exit from the loop and choose a smaller orbit (in this case the algorithm restarts from **Step 1**), or increase the constellation size (in this case the algorithm restarts from **Step 3**). The user predefines this choice.

end

end

Acknowledgments

Dr. Camilla Colombo acknowledges the support received by the EU Marie Curie grant 302270 (SpaceDebECM - Space Debris Evolution, Collision risk, and Mitigation) within the European FP7 framework at the Department of Aerospace Science and Technology, Politecnico di Milano, Italy. Michele Stramacchia would like to acknowledge Dr. Toal from the University of Southampton for his support. The author would like to acknowledge the anonymous reviewer whose comments improved the quality of the paper.

References

ANDRONIKOV, A., LAURETTA, D., HIL, D. & ANDRONIKOVA, I. 2014. Vesicle-metal-sulfide assemblages from the Chelyabinsk meteorite. *In:* MUINONEN, K., PENTTILA, A., GRANVIK, M., VIRKKI, A., FEDORETS, G., WILKMAN, O. & KOHOUT, T. (eds.) *Asteroids, Comets, Meteors - Book of Abstracts, Helsinki, Finland, 2014.*

BATTIN, R. H. 1999. *An Introduction to the Mathematics and Methods of Astrodynamics,* 1801 Alexander Bell Drive, Reston, VA 20191, AIAA, 1999.

BELTON, J. S. 2004. *Mitigation of Hazardous Comets and Asteroids,* Cambridge, Cambridge University Press.

BERNELLI ZAZZERA, F., TOPPUTO, F. & MASSARI, M. 2004. Assessment of Mission Design Including Utilization of Libration Points and Weak Stability Boundaries. Department of Aerospace Engineering, Politecnico di Milano, Italy.

BINZEL, R. P., GEHRELS, T. & MATTHEWS, M. S. 1989. *Asteroids 2,* Tucson, University of Arizona Press.

BUCHHEIM, R. K. Methods and Lessons Learned Determining The H-G Parameters Of Asteroids Phase Curves. *In:* WARNER, B. D., FOOTE, J. & BUCHHEIM, R., eds. The Society for Astronomical Sciences 29th Annual Symposium on Telescope Science, May 11-13 2010 Big Bear Lake, CA. Society for Astronomical Sciences, Inc., 101-115.

DEMEYER, J. & GURFIL, P. 2007. Transfer to Distant Retrograde Orbits Using Manifold Theory. *Journal of Guidance, Control, and Dynamics,* 30**,** 1261-1267.

DUNHAM, D. W., REITSEMA, H. J., LU, E., ARENTZ, R., LINFIELD, R., CHAPMAN, C., FARQUHAR, R., LEDKOV, A. A., EISMONT, N. A. & CHUMACHENKO, E. 2013. A concept for providing warning of earth impacts by small asteroids. *Solar System Research,* 47**,** 315-324.

DUTT, P. & SHARMA, R. K. 2012. On the evolution of the *f* family in the restricted three-body problem. *Astrophysics and Space Science,* 340**,** 63-70.
DYMOCK, R. 2010. *Asteroids and Dwarf Planets and How to Observe Them*, Springer New York.
HÉNON, M. 1969. Numerical Exploration of the Restricted Problem V *Astronomy and Astrophysics,* 1**,** 223-238.
HÉNON, M. 1997. *Generating Families In The Restricted Three-Body Problem*, Springer-Verlag Berlin, Germany, Springer Science & Business Media, 1 Jul 2003. .
KECHICHIAN, J. A., CAMPBELL, E. T., WERNER, M. F. & ROBINSON, E. Y. 2005. Solar Surveillance Zone Population Strategies With Picosatellites Using Halo And Distant Retrograde Orbits. *Acta Astronautica,* 56**,** 495-506.
KOON, W. S., LO, M. W., MARSDEN, J. E. & ROSS, S. D. 2011. *Dynamical Systems the Three-Body Problem and Space Mission design*, Springer-Verlag New York.
LAM, T. & WHIFFEN, G. J. 2005. Exploration of Distant Retrograde Orbits Around Europa. *In:* AAS/AIAA (ed.) *Space Flight Mechanics Meeting.* Copper Mountain, Colorado.
LUU, J. & JEWITT, D. 1989. On the relative numbers of C types and S types among near-earth asteroids. *Astronomical Journal,* 98**,** 1905-1911.
MEYER, K. R., HALL, G. R. & OFFIN, D. 2009. *Introduction to Hamiltonian Dynamical Systems and the N-Body Problem*, New York, Springer Science+Business Media.
MICHELSEN, R. 2004. *Near-Earth Asteroids from Discovery to Characterisation.* Doctoral Thesis, University of Copenaghen.
MICHELSEN, R., HAACK, H., ANDERSEN, A. C. & JORGENSEN, J. L. Asteroid and NEA detection models. Proceedings of the International Conference on Recent Advances in Space Technologies, November 20-22 2003 Istanbul, Turkey. IEEE, 247-252.
MINGOTTI, G. P. 2010. *Trajectory Design and Optimization in Highly Nonlinear Astrodynamics.* Doctoral Thesis, Department of Aerospace Engineering, Politecnico di Milano, Italy.
MINGOTTI, G. P., TOPPUTO, F. & BERNELLI ZAZZERA, F. 2010. Exploiting Distant Periodi Orbits and their Invariant manifolds to design novel space trajectories to the moon. *In:* MORTARI, D., STARCHVILLE, T. F., TRASK, A. J. & MILLER, J. K. (eds.) *Spaceflight Mechanics 2010.* San Diego, California: Univelt Inc.
MURRAY, C. D. & DERMOTT, S. F. 1999. *Solar System Dynamics,* Cambridge, Cambridge University Press.
PERKO, L. 2013. *Differential Equations and Dynamical Systems*, Springer New York.
PERNA, D., BARUCCI, M. A. & FULCHIGNONI, M. 2013. The near-Earth objects and their potential threat to our planet. *The Astronomy and Astrophysics Review,* 21**,** 1-28.
SANCHEZ, J. P. & COLOMBO, C. 2013. Impact Hazard Protection Efficiency by a Small Kinetic Impactor. *Journal of Spacecraft and Rockets,* 50**,** 380-393.
SCOTT, C. J. & SPENCER, D. B. 2010. Calculating Transfer Families to Periodic Distant Retrograde Orbits Using Differential Correction. *Journal of Guidance, Control, and Dynamics,* 33**,** 1592-1605.
STOKES, G. H. 2003. Study to Determine the Feasibility of Extending the Search for Near-Earth Objects to Smaller Limiting Diameters. National Aeronautics and Space Administration, Research Report 030825.
STOKES, G. H., EVANS, J. B. & LARSON, S. M. 2002. Near-Earth Asteroid Search Programs. *In:* BOTTKE, W. F., CELLINO, A., PAOLICCHI, P. & BINZEL, R. P. (eds.) *Asteroids 3.* Tucson, University of Arizona Press.
STRAMACCHIA, M. 2013. *Distant Periodic Orbits For Asteroid Detection.* Master Thesis, Department of Aerospace Engineering, Politecnico di Milano, Italy.
SZEBEHELY, V. 1967. *Theory of Orbits: The Restricted Problem of Three Bodies*, ACADEMIC PRESS INC., London, Elsevier, 2012.
THURMAN, R. & WORFOLK, P. A. 1996. The geometry of Halo orbits in the circular restricted three-body problem. The Geometry Center: Technical Report GCG95, University of Minnesota.
TODD, M., TANGA, P., COWARD, D. M. & ZADNIK, M. G. 2011. An optimal Earth Trojan asteroid search strategy. *Mon.Not.R.Astron.Soc. 420 (2012) L28-32.*
TODD, M., TANGA, P., COWARD, D. M. & ZADNIK, M. G. 2012. An optimal Mars Trojan asteroid search strategy. *Mon.Not.R.Astron.Soc. 424 (2012) 372-376.*
VALSECCHI, G. B., PEROZZI, E. & ROSSI, A. A space mission to detect imminent Earth impactors. High-lights of Astronomy, August 2012. Proceedings of the International Astronomical Union, 488-489.
VEEDER, G. J., TEDESCO, E. F., FOWLER, J. W. & CHILLEMI, J. R. 1992. The IRAS Minor Planet Survey. Technical Report PL-TR-92-2049, Phillips Laboratory, Hanscom Air Force Base, MA.
VEREŠ, P., JEDICKE, R., WAINSCOAT, R., GRANVIK, M., CHESLEY, S., ABE, S., DENNEAU, L. & GRAV, T. 2009. Detection of Earth-impacting asteroids with the next generation all-sky surveys. *Icarus 203:472-485,2009.*
VINTI, J. P., DER, G. J. & BONAVITO, N. L. 1998. *Orbital and celestial mechanics,* Los Angeles, California, American Institute of Aeronautics and Astronautics.
WERNER, S. C., HARRIS, A. W., NEUKUM, G. & IVANOV, B. A. 2002. The Near-Earth Asteroid Size–Frequency Distribution: A Snapshot of the Lunar Impactor Size–Frequency Distribution. *Icarus,* 156**,** 287-290.
WOOLLEY, R. C. & SCHEERES, D. J. 2010. Hyperbolic Periodic Orbits in the Three-Body Problem and their Application to Orbital Capture. *Born Symposium.* Boulder, Colorado.
XUE, M. & JUNFENG, L. 2013. Distant quasi-periodic orbits around Mercury. *Astrophysics and Space Science,* 343**,** 83-93.
ZULUAGA, J. I. & FERRIN, I. 2013. A preliminary reconstruction of the orbit of the Chelyabinsk Meteoroid. *ArXiv e-prints.*